



# Particle Acceleration in Strong Turbulence in the Earth's Magnetotail

R. E. Ergun<sup>1,2</sup> , N. Ahmadi<sup>2</sup>, L. Kromyda<sup>1,2</sup>, S. J. Schwartz<sup>2</sup>, A. Chasapis<sup>2</sup>, S. Hoilijoki<sup>2</sup>, F. D. Wilder<sup>2</sup>, P. A. Cassak<sup>3</sup> , J. E. Stawarz<sup>4</sup> , K. A. Goodrich<sup>5</sup>, D. L. Turner<sup>6</sup>, F. Pucci<sup>2</sup>, A. Pouquet<sup>2</sup>, W. H. Matthaeus<sup>7</sup> , J. F. Drake<sup>8</sup> , M. Hesse<sup>9</sup>, M. A. Shay<sup>7</sup> , R. B. Torbert<sup>10,11</sup>, and J. L. Burch<sup>11</sup>

<sup>1</sup> Department for Astrophysical and Planetary Sciences, University of Colorado, Boulder, CO, USA

<sup>2</sup> Laboratory of Atmospheric and Space Sciences, University of Colorado, Boulder, CO, USA

<sup>3</sup> West Virginia University, Morgantown, WV, USA

<sup>4</sup> The Blackett Laboratory, Imperial College London, UK

<sup>5</sup> Space Sciences Laboratory, University of California, Berkeley, CA, USA

<sup>6</sup> Johns Hopkins University Applied Physics Laboratory, Laurel, MD, USA

<sup>7</sup> University of Delaware, Newark, DE, USA

<sup>8</sup> University of Maryland, College Park, MD, USA

<sup>9</sup> Birkeland Centre For Space Science, University of Bergen, Bergen, Norway

<sup>10</sup> University of New Hampshire, Durham, NH, USA

<sup>11</sup> Southwest Research Institute, San Antonio, TX, USA

Received 2020 February 6; revised 2020 May 21; accepted 2020 June 6; published 2020 August 4

## Abstract

In many space, astrophysical, and laboratory plasmas the energy contained in the magnetic field or plasma flow exceeds the thermal energy. Magnetic field ( $\mathbf{B}$ ) annihilation, often enabled by magnetic reconnection, transfers magnetic energy to particles. Shocks transfer bulk flow energy to particles. If there is a sufficiently large energy transfer, strong turbulence ( $|\delta\mathbf{B}|/|\mathbf{B}| \sim 1$ ) develops, which, in turn, can result in nonthermal acceleration. In this article, we investigate acceleration in a finite-sized region of strong turbulence driven by magnetic reconnection with analytical modeling and test-particle simulations. This research is based on detailed observations in the Earth's magnetotail. We find that the primary transfer of magnetic energy to particle energy is advanced by large-amplitude electric field structures ( $\mathbf{E}$ ) generated by the strong turbulence. To no surprise, ion energization is dominated by intense DC  $\mathbf{E}$ ,  $\mathbf{E}$  near the ion cyclotron frequency ( $f_{ci}$ ), and/or  $\mathbf{E}$  variations at scales near the ion gyroradius. Electron energization comes from higher-frequency  $\mathbf{E}$ . The turbulent cascade continuously regenerates  $\mathbf{E}$  near  $f_{ci}$  and higher frequencies. Importantly, the turbulence also creates magnetic depletions that can trap particles and considerably increase their dwell time in regions of strong energization, which substantially enhances nonthermal acceleration. Moreover, energization is primarily perpendicular to  $\mathbf{B}$ , so particles have difficulty escaping regions of depleted  $\mathbf{B}$ , which can lead to near runaway acceleration. We discuss how this process may be active in large-scale settings such as supernova shells and may contribute, at least in part, to the development of the cosmic ray spectrum.

*Unified Astronomy Thesaurus concepts:* Space plasmas (1544)

## 1. Introduction

Active plasmas such as stellar winds (e.g., Goldstein et al. 1994; Alexandrova et al. 2012), supernova remnants (e.g., Chevalier 1977), accretion disks (e.g., Quataert & Gruzinov 1999), the interstellar medium (e.g., Goldreich & Sridhar 1995), stellar atmospheres (e.g., Cranmer et al. 2015), pulsar magnetospheres (Arons 2012), and magnetospheres (e.g., Borovsky et al. 1997; Weygand et al. 2005; Chasapis et al. 2015; Stawarz et al. 2016; Breuillard et al. 2018 and references therein) are understood to contain regions of strong turbulence in which  $|\delta\mathbf{B}|/|\mathbf{B}| \sim 1$ , where  $\mathbf{B}$  is the magnetic field. The energy source for turbulence is often magnetic field annihilation that is enabled by magnetic reconnection (e.g., Drake et al. 2006; Eastwood et al. 2009; Ergun et al. 2015; Price et al. 2016, 2017) or braking of a high-Mach plasma flow at a shock front (see Blandford & Eichler 1987 and references therein). It is important to realize that for both of these processes the resulting turbulence occupies a significantly larger volume than does the thin layer in which these processes occur. Magnetic reconnection enables magnetic field annihilation over a much larger volume than the diffusion regions occupy (e.g., Ergun et al. 2018). Turbulence generated by a shock often extends downstream into a region many times the thickness of the shock (e.g., Schwartz & Burgess 1991).

Accelerated particles have long been associated with shocks (see Blandford & Eichler 1987). The observation of accelerated particles upstream of the Earth's bow shock initiated a debate over their origin (e.g., Gosling et al. 1978, 1989). It is now generally agreed that, while shock reflection is active (e.g., Turner et al. 2018), the majority of the accelerated particles appear to come from either from the magnetosheath (shocked solar wind) or the magnetotail. Accelerated particles have also been associated with magnetic reconnection (Øieroset et al. 2002; Drake et al. 2006; Jaynes et al. 2016; Oka et al. 2018).

Recently, the Magnetospheric Multiscale mission (MMS, Burch et al. 2016) has led to a flurry of new results regarding detailed kinetic processes that underlie magnetic reconnection, acceleration, and turbulence. A connection between magnetic reconnection, turbulence, and particle acceleration is emerging (Jaynes et al. 2016; Ergun et al. 2018), as well as a connection between shocks, turbulence, and particle acceleration (Turner et al. 2018).

This article follows a companion paper (Ergun et al. 2020, herein called the [companion paper](#)) that describes observations of particle heating and acceleration inside of an extended region of strong turbulence driven by magnetic field annihilation that is enabled by magnetic reconnection. In

these two articles, we find that strong turbulence creates an ideal setting for particle acceleration. Observations ([companion paper](#)) indicate that a number of energization processes are active. Ion energization in a current sheet from quasi-adiabatic orbits and/or chaotic orbits is certainly active (Speiser 1965). Other energization mechanisms include, but are not limited to, cyclotron-resonant/gyro-resonant energization (e.g., Chang et al. 1986), second order heating, Fermi acceleration (Drake et al. 2006), betatron acceleration, double layers (e.g., Ergun et al. 2009), and a variety of wave-resonant processes. Some of these processes by themselves promote acceleration. However, a central conclusion of this work is that trapping in magnetic depletions inhibits a particle's ability to escape the turbulent region and thereby appreciably enhances nonthermal acceleration. Furthermore, observations suggest that perpendicular (to the magnetic field,  $\mathbf{B}$ ) energization dominates and tends to favor energetic particles, so magnetically trapped particles tend to remain trapped, leading to near runaway energization.

A key aspect of the observations is the very existence of magnetic depletions, particularly in regions of strong turbulence. While  $\mathbf{B}$  depletions on MHD scales have been known for decades and suspected to be associated with acceleration (e.g., Matthaeus et al. 1984), MMS and other space plasma missions now show that  $\mathbf{B}$  depletions with  $|\delta\mathbf{B}|/|\mathbf{B}| \sim 1$  down to small scales are frequently observed in regions of strong turbulence (e.g., Goodrich et al. 2016a, 2016b; Huang et al. 2017). Clearly, such depletions suggest the presence of some degree of compressional turbulence in addition to Alfvénic turbulence.

This article is based primarily on analytical and test-particle modeling. Test-particle simulations are in a 1D spatial domain that tracks momentum in 3D. While not self-consistent, they give good insight into the trapping and acceleration process, which is difficult to analytically model. The test-particle simulations are constructed to reproduce a realistic electric field ( $\mathbf{E}$ ) and magnetic field environment in the turbulent region. The results are compared to analytic estimates when possible. While the simulations are very basic, they illuminate the consequence of trapping in  $\mathbf{B}$  depletions.

## 2. Summary of Observations

The observations are presented in the [companion paper](#), so our discussion is brief. For convenience, we replot a magnified view of the turbulence event in Figures 1(a)–(h), an interpretation of the turbulent region and its estimated size in Figure 1(i), the characteristics of the  $\mathbf{E}_{ac}$  ( $\mathbf{E}$  with  $f > 0.25$  Hz, where  $f$  is frequency) in Figures 1(j)–(m), and the average plasma conditions in Figure 1(n). This turbulent event is considered strong ( $|\delta\mathbf{B}|/|\mathbf{B}| \sim 1$ , Figure 1(e)) and intermittent (Figure 3 of the [companion paper](#)). A description of MMS and its instruments can be found in a series of articles (Burch et al. 2016; Ergun et al. 2016; Le Contel et al. 2016; Lindqvist et al. 2016; Mauk et al. 2016; Pollock et al. 2016; Russell et al. 2016; Torbert et al. 2016).

To summarize, at approximately 2017 July 26 07:22 UT, a region of strong turbulence engulfed the MMS spacecraft, which are in the magnetotail roughly  $23 R_E$  from Earth. At  $\sim 07:20$  UT a flow reversal (Figure 1(g), blue trace) and a reversal of  $B_z$  (Figure 1(e), red trace; difficult to see by eye) signaled that a magnetic reconnection event was near the center of the turbulent region (e.g., Nagai et al. 1998; Øieroset et al. 2001; Torbert et al. 2018). The turbulent region retreated away

from Earth and the MMS satellites no longer detect strong turbulence after  $\sim 07:38$  UT.

Figures 1(a) and (b) indicate ion heating from  $\sim 4$  keV outside of the turbulent region to  $\sim 20$  keV inside of the region and acceleration to greater than 300 keV. Electrons energize from  $\sim 1$  keV outside of the region to  $\sim 5$  keV inside of the region with an accelerated tail up to  $\sim 200$  keV (Figures 1(c) and (d)). Throughout the region there are strong fluctuations in  $\mathbf{B}$  (Figure 1(e)) and large-amplitude fluctuations in  $\mathbf{E}$  (Figure 1(f)). Given the ion flows (Figure 1(g)),  $|\mathbf{E}|$  should peak at  $\sim 20$  mV m $^{-1}$ , whereas the observations indicate 10 times higher amplitudes. Importantly, there is a significant density depletion in the turbulent region (Figure 1(h)).

MMS also measures current ( $\mathbf{J}$ ), allowing for a determination of  $\mathbf{J} \cdot \mathbf{E}$ . The details of  $\mathbf{J} \cdot \mathbf{E}$  for this event have been reported earlier (Ergun et al. 2018). Updated results after a recalibration of  $\mathbf{E}$  (minor differences) are summarized in Table 1. To understand Table 1, it is important to recognize that  $\mathbf{E}$  can have a baseline offset (accuracy) of  $\sim \pm 1$  mV m $^{-1}$  on any given measurement, whereas it has much better precision (the uncertainty between measurements less than  $\sim 2$  s apart is less than 0.1 mV m $^{-1}$ ; Ergun et al. 2016; Lindqvist et al. 2016; Torbert et al. 2016). The primary conclusions from the  $\mathbf{J} \cdot \mathbf{E}$  study are:

(1)  $\langle \mathbf{J} \cdot \mathbf{E} \rangle / \langle n \rangle$  is roughly 2–3 keV s $^{-1}$  per particle pair and is dominated by the perpendicular contribution (the averaging is over the turbulent region in Ergun et al. 2018). A parallel contribution cannot be ruled out due to the uncertainty from the baseline offsets. It is suggested, but not fully proven, that ions are the primary recipients of the low-frequency energy.

(2)  $(\langle \mathbf{J} \cdot \mathbf{E} \rangle - \langle \mathbf{J} \rangle \cdot \langle \mathbf{E} \rangle) / \langle n \rangle$ , the fluctuating contribution of  $\langle \mathbf{J} \cdot \mathbf{E} \rangle$ , can be derived with less uncertainty and is such that the perpendicular contribution is roughly 80% of its total value.

(3) It is suggested, but not fully proven, that electrons are the primary recipients of the net fluctuating contribution of  $\langle \mathbf{J} \cdot \mathbf{E} \rangle$ , which may be up to  $\sim 660$  keV s $^{-1}$  per particle (Table 1).

In this article, we break  $\mathbf{E}$  into two spectral domains. The “DC/cyclotron” band ( $f \leq 0.25$  Hz) includes most of the power at the ion cyclotron frequency ( $f_{ci}$ ), which is often ( $>95\%$  of the time) between 0.05 and 0.25 Hz and averages  $\sim 0.15$  Hz. The “AC” band ( $\mathbf{E}_{ac}$ ) includes  $f > 0.25$  Hz, which excludes most of the power at  $f_{ci}$ .  $\mathbf{E}_{ac}$  has a defined correlation of time of  $\sim 24$  ms (Figure 1(j)) and a defined correlation distance of  $\sim 48$  km (Figure 1(k)), which are consistent with intermittent structure with speeds of roughly  $2000$  km s $^{-1} \pm 1000$  km s $^{-1}$  (the [companion paper](#)).

$E_{\parallel}$  and  $E_{\perp}$  are dissimilar and their cross-correlation magnitude is  $<0.1$ , so  $E_{\parallel}$  and  $E_{\perp}$  are treated separately. Figures 1(l)–(m) display, respectively, the probability distribution functions (PDFs) of  $|E_{\parallel ac}|$  and  $|E_{ac}|$ . The PDFs have nearly the same profile, but the PDF of  $|E_{\parallel ac}|$  is weaker. They are fit well by an exponential:

$$P(|E|) \propto e^{-\sqrt{|E|/E_0}} \quad (1)$$

with  $E_0 = 1.34$  mV m $^{-1}$  for  $E_{\perp}$  and  $E_0 = 0.82$  mV m $^{-1}$  for  $E_{\parallel}$  (Figure 1(l)). The authors are unaware of a theoretical justification for this analytical form.

A relevant result of the statistical study of  $\mathbf{E}$  in the [companion paper](#) is that there is a fairly well-defined correlation time and a fairly well-defined correlation distance in  $\mathbf{E}_{ac}$ . Combined with the analytical fits of the PDFs,  $\mathbf{E}_{ac}$  can be

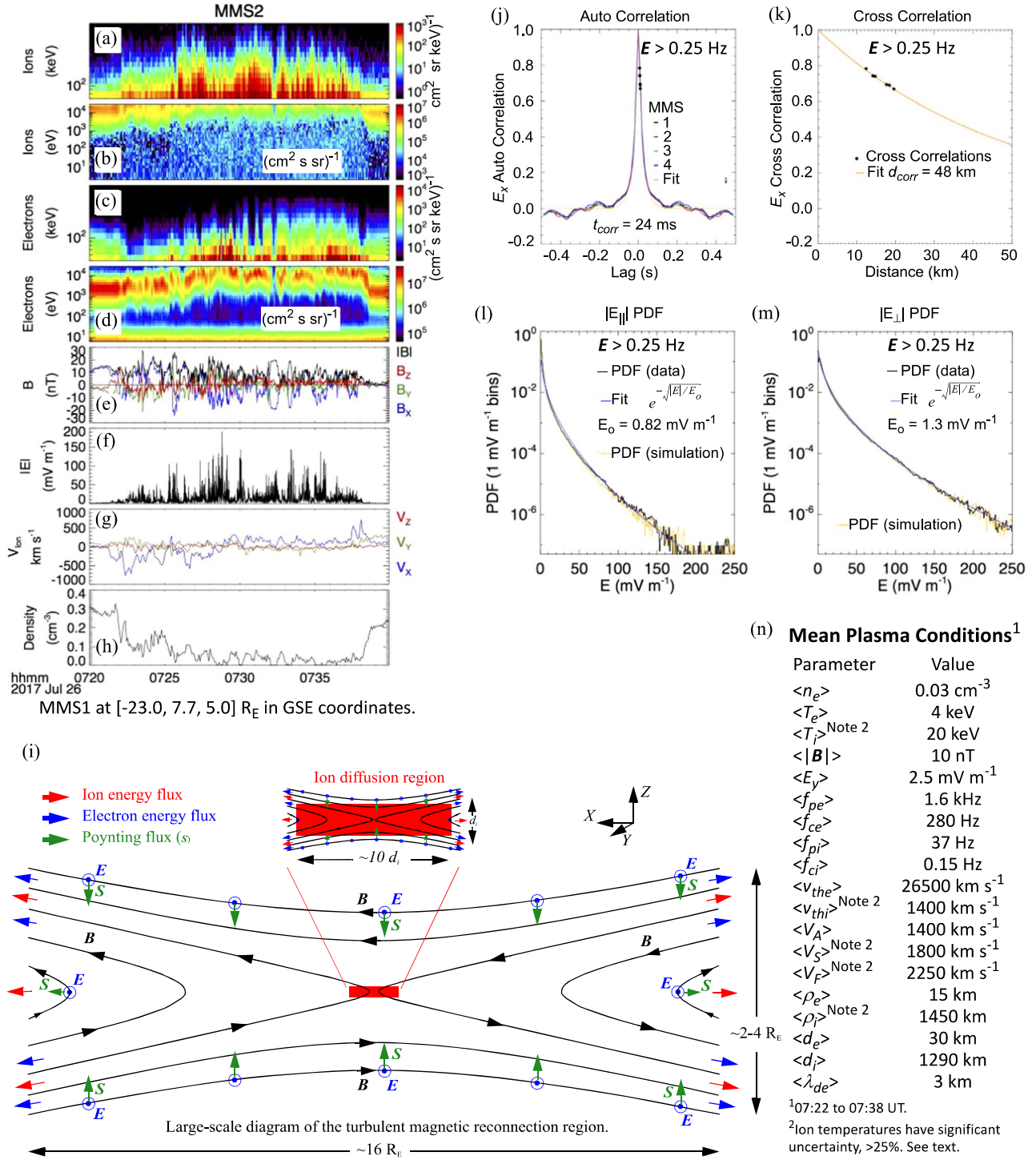


**Figure 1.** A review of observations by the MMS satellites. The location of MMS1 is below the horizontal axis. (a) The omni-directional ion intensity as a function of energy (vertical axis, 60–600 keV) and time (horizontal axis). Data from all four MMS spacecraft are combined to form this plot. (b) The omni-directional ion differential energy flux as a function of energy (10 eV–25 keV) and time. (c) The omni-directional electron intensity as a function of energy (50–500 keV) and time. (d) The omni-directional electron differential energy flux as a function of energy (10 eV–25 keV) and time. (e) Vector  $B$  in GSE coordinates. The color code is to the right of the box.  $X$  is toward the Sun,  $Z$  is normal to the ecliptic, and  $Y$  completes the system. The turbulence imparts strong variations in  $|B|$  (black trace). (f)  $|E|$ . The amplitudes of  $E$  are more than 10 times that expected from MHD turbulence. (g) The three components of  $V_{\text{ion}}$  in GSE coordinates.  $V_x$  (blue trace) is consistent with a magnetic reconnection jet. It reverses direction at  $\sim 07:28$  UT indicating that a magnetic reconnection region passed by the MMS satellites at that time. (h) The electron density. The accuracy degrades if  $n_e < 0.03 \text{ cm}^{-3}$ . (i) An interpretation of the turbulent region, which, by volume, is far larger than the diffusion region of magnetic reconnection. Magnetic reconnection enables Poynting flux entry to the system on the order of  $3 \text{ keV s}^{-1}$  per particle pair. We postulate that this Poynting flux (from  $B$  annihilation) is driving the turbulence. (j) An autocorrelation of  $E_{ac}$  ( $E$  with  $f > 0.25$  Hz) indicates a defined correlation time of 24 ms. (k) A cross-correlation of  $E_{ac}$  between spacecraft indicates a defined correlation distance of 48 km. (l) The probability distribution function (PDF) of  $|E_{\parallel}|$  and a fit to a stretched exponential,  $e^{-\sqrt{|E|/E_0}}$ , where  $E_0 = 0.82 \text{ mV m}^{-1}$ . (m) The PDF of  $E_{ac}$  and a fit to a stretched exponential. (n) Basic plasma parameters.

**Table 1**  
Summary of  $\mathbf{J} \cdot \mathbf{E}$  Measurements

Quantity	Value ( $\text{pW m}^{-3}$ )				Value/ $\langle n \rangle$ ( $\text{eV s}^{-1}$ )			
	Total	Perp.	Par.	$\pm$	Total	Perp.	Par.	$\pm$
$\langle \mathbf{J} \cdot \mathbf{E} \rangle$	16.5	15.8	0.7	5.0	3440	3290	150	1040
$\langle \mathbf{J} \rangle \cdot \langle \mathbf{E} \rangle$	13.3	13.3	0.0	5.0	2780	2780	0	1040
$\langle \mathbf{J} \cdot \mathbf{E} \rangle - \langle \mathbf{J} \rangle \cdot \langle \mathbf{E} \rangle$	3.1	2.4	0.7	0.25	660	510	150	50
$\langle \mathbf{J}_F \cdot \mathbf{E}_F \rangle$	1.2	0.6	0.6	0.25	250	130	120	50

**Note.** The values of  $\langle \mathbf{J} \cdot \mathbf{E} \rangle$  in this table have small differences from Ergun et al. (2018) due to the recalibration of  $\mathbf{E}$ .  $\mathbf{J}_F$  and  $\mathbf{E}_F$  are filtered to  $>0.5$  Hz, whereas  $f_{ci}$  varies from  $<0.1$  Hz to  $\sim 0.3$  Hz.

reproduced to realistically examine electron energization and, with additional treatment, ion energization.

### 3. Electron Energization

We begin by examining electron energization. At first glance, observations (the [companion paper](#)) suggest that parallel processes govern thermal heating of electrons ( $\sim 4$  keV to  $\sim 5$  keV), whereas perpendicular energization appears to produce a nonthermal tail ( $\gtrsim 50$  keV). The observations also suggest that electron energization can come from the unusually large-amplitude  $\mathbf{E}_{ac}$  combined with trapping in  $\mathbf{B}$  depletions.

The electron temperature ( $T_e$ ) inside of the turbulent region often has  $T_{e\parallel} > T_{e\perp}$  in the thermal core, which is inconsistent with the observation that  $\langle \mathbf{J} \cdot \mathbf{E} \rangle_{\parallel} \ll \langle \mathbf{J} \cdot \mathbf{E} \rangle_{\perp}$ . Furthermore, the portion of  $\langle \mathbf{J} \cdot \mathbf{E} \rangle$  that electrons receive, estimated to be  $< 660 \text{ eV s}^{-1}$ , is insufficient to energize transiting electrons from  $\sim 1$  to  $\sim 5$  keV. An electron with a parallel energy ( $W_{e\parallel}$ ) of approximately 2.5 keV ( $v_{e\parallel} \sim 3 \times 10^7 \text{ m s}^{-1}$ ) can traverse the turbulent region ( $\sim 16 R_E$  or  $\sim 10^8 \text{ m}$ ; Figure 1(i)) in approximately 3 s. One can quickly surmise that the measured  $\langle \mathbf{J} \cdot \mathbf{E} \rangle_{\parallel}$  cannot explain the measured  $T_{e\parallel}$  ( $\sim 5$  keV) without a trapping or nonlinear mechanism.

In this article,  $T_e$  (or  $T_i$ ) represents the second moment of a distribution (minus bulk flow), whereas  $W_e$  (or  $W_i$ ) is the kinetic energy of an individual particle. At times, we refer to a “core” temperature ( $T_{\text{core}}$ ) or a “reference” temperature ( $T_{\text{ref}}$ ).  $T_{\text{core}}$  is a fit of the low-energy (thermal) part of a distribution to a Maxwellian distribution ignoring a nonthermal tail, so  $T_{\text{core}} \leq T_e$ . A Maxwellian distribution is often included in plots to visually highlight nonthermal acceleration.

#### 3.1. Electron Test-particle Simulations with $\mathbf{B}$ Constant

To understand electron energization, we follow a set of electrons as they traverse a turbulent region using a 1D, relativistic, test-particle simulation based on a code that tracks velocities in 3D and allows electrons to gyrate in an imposed  $\mathbf{B}$  and accelerate in an imposed  $\mathbf{E}$  (Ergun et al. 2010; see Marchand et al. 2014 for verification). The spatial domain is limited to 1D due to the large size of the turbulent region, which requires some modifications from the 2D and 3D codes (Ergun et al. 2010). Parallel forces include an imposed  $E_{\parallel}$  and a magnetic mirror force,  $\mu \nabla_{\parallel} B_{\parallel}$ , where  $\mu = p_{\perp}^2 / 2m_e |\mathbf{B}|$ ,  $\mathbf{p}$  is momentum, and  $m_e$  is electron mass. Perpendicular evolution occurs in two steps using a Boris-like algorithm (Boris 1970). The first step advances particles under the influence of  $\mathbf{B}$  while conserving  $\mu$ . Subsequently,  $\mathbf{p}_{\perp}$  is advanced by the imposed  $\mathbf{E}_{\perp}$ , which can break the first adiabatic invariant ( $\mu$ ). The algorithms

(e.g., Northrop 1963; Elkington et al. 2002, 2004) work well in classical and relativistic systems.

A 1D test-particle simulation has several advantages and, of course, several obvious limitations (e.g., it is not self-consistent). Since  $\mathbf{E}$  and  $\mathbf{B}$  are imposed, there is no spurious behavior at the boundaries. Distribution functions and kinetic behavior are easily diagnosed. Our test-particle simulations have open boundaries, which are essential for a realistic investigation of energization in a finite-sized region. Electrons can pass through a  $16 R_E$  turbulent region in a few seconds, whereas the turbulence endures for over 18 minutes. The open boundaries (Figure 2(a)) require that electron fluxes continuously enter (and exit) from the left and right boundaries from (and into) an ambient population outside of the turbulent region with  $T_e = 1$  keV.

A realistic reproduction of the imposed  $\mathbf{E}$  is essential. The observations (the [companion paper](#)) reveal a reasonably well-defined correlation distance ( $d_{\text{corr}} \sim 48 \text{ km}$ ), correlation time ( $t_{\text{corr}} \sim 24 \text{ ms}$ ), and PDF of  $\mathbf{E}_{ac}$  ( $f > 0.25 \text{ Hz}$ ), which we use to generate  $E_{ac\parallel}$  and  $\mathbf{E}_{ac\perp}$ . The measured  $t_{\text{corr}}$  (24 ms) is mostly inconsequential for electrons because a thermal electron traverses  $d_{\text{corr}}$  in  $\sim 2 \text{ ms}$ . Details are in the [Appendix](#).

For the initial run,  $\mathbf{B}$  is constant. The simulation domain (Figure 2(a)) extends from  $-10 R_E$  to  $+10 R_E$  and is initiated with a normalized electron density ( $n_e$ ) of 1 and  $T_e = 1$  keV, representing the ambient magnetotail.  $\mathbf{E}_{ac}$  is imposed only in the turbulent region, which lies between  $-8 R_E$  and  $+8 R_E$ . Figure 2(b) plots the electron phase-space density (averaged over 0.5 s) at  $t = 10 \text{ s}$  versus  $p_{e\parallel}$  and distance. We normalize  $p_{e\parallel}$  to the thermal momentum ( $p_{\text{eth}}$ ) with  $T_e = 1$  keV. Figure 2(c) displays  $T_{e\parallel}$  and  $T_{e\perp}$  as a function of distance, and Figure 2(d) plots the normalized density ( $n_e$ ) as a function of distance; the colors represent times. One can see that  $T_{e\parallel}$  is higher than  $T_{e\perp}$  in the turbulent region. As  $T_{e\parallel}$  and  $T_{e\perp}$  increase,  $n_e$  decreases. At  $t = 10 \text{ s}$ ,  $n_e$  decreases a short distance into the turbulent region to about 25% of the ambient density.

Figure 2(e) shows the time evolution of the average of  $T_{e\parallel}$  and  $T_{e\perp}$  in the simulation. One can see an initial rapid rise in  $T_{e\parallel}$ , whereas  $T_{e\perp}$  develops more slowly in time. After 10 s, there is little change in the electron distributions (the simulations have been carried to 60 s). This simulation reaches a quasi-equilibrium state.

The density depletion (Figure 2(d),  $t = 10 \text{ s}$ ) and what appears to be a rapid rise in  $T_{e\parallel}$  (Figure 2(c)) are also seen in the observations (Figure 1). As stated in the [companion paper](#), the observation that  $T_{e\parallel} > T_{e\perp}$  in the thermal core is an enigma, since the parallel contribution of  $\mathbf{J} \cdot \mathbf{E}$  is observed to be small. However, the simulation gives us good insight into this enigma. It also shows that  $T_{e\parallel} > T_{e\perp}$  with relatively little energy transfer

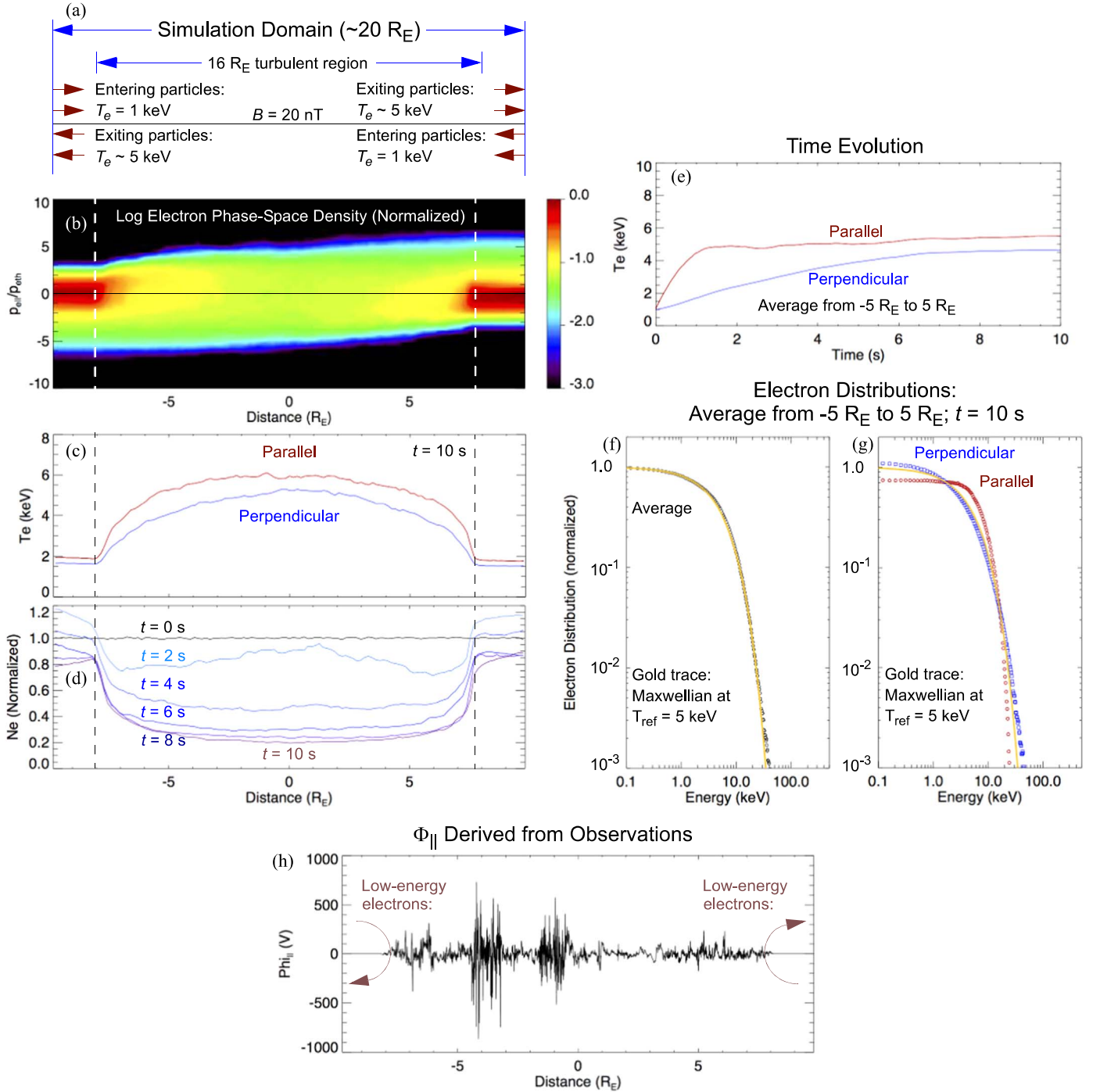


**Figure 2.** (a) A 1D spatial, 3D velocity test-particle simulation.  $B$  is constant at  $+20$  nT.  $E_{ac}$  is reproduced using the measured  $d_{\text{corr}}$ ,  $t_{\text{corr}}$ , and PDF. The simulation domain extends approximately  $\pm 10 R_E$  and is initiated with a 1 keV electron population at a normalized density of 1. Inside of the simulation domain, the turbulent region is  $\pm 8 R_E$  ( $10^8$  m) and is marked with vertical dashed lines. A 1 keV electron population is at the two boundaries. (b) The normalized electron phase-space density at  $t = 10$  s. A large fraction of low-energy electrons are reflected as they enter the turbulent region due to fluctuating potentials. The raw image is 125 pixels in distance and 50 pixels in  $p_{\parallel}$  and smoothed to higher resolution. (c)  $T_{e\parallel}$  and  $T_{e\perp}$  as a function of distance at 10 s. (d) The density as a function of distance. The colors represent time. (e)  $T_{e\parallel}$  and  $T_{e\perp}$  as a function of time. (f) and (g) The normalized electron distribution as a function of energy. The black trace is averaged over all directions. The blue trace is  $f(p_{e\perp})$ , the red trace is  $f(p_{e\parallel})$ , and the gold trace is a Maxwellian distribution with  $T_e = 5$  keV. There is no significant nonthermal tail, indicating little nonthermal acceleration. (h) An example of  $\Phi_{\parallel}$  derived from observations. The fluctuations in  $\Phi_{\parallel}$  reflect a large portion of low-energy electrons entering the turbulent region.

via the parallel contribution of  $\mathbf{J} \cdot \mathbf{E}$ . We estimate that, after an initial surge at the simulation start (up to  $\sim 5$  s),  $\langle \mathbf{J} \cdot \mathbf{E} \rangle_{\parallel} / \langle n \rangle \sim 200$  eV  $s^{-1}$  per electron.

The apparent parallel electron heating comes from what we call a “ $\Delta\Phi_{\parallel}$  filter.” The defined correlation distance ( $d_{\text{corr}}$ ) has a subtle but important impact on the parallel motion of

electrons. Since the time for an electron to traverse  $d_{\text{corr}}$  ( $\sim 2$  ms) is far less than  $t_{\text{corr}}$  ( $\sim 24$  ms), temporal changes do not have a large impact. As a result, one must treat the electron evolution as a series of encounters with random potential structures,  $\Delta\Phi_{\parallel}$ , rather than a series of random  $E_{\parallel}$ .

Figure 2(h) plots an example of  $\Phi_{\parallel}$  that an electron may experience as it traverses the turbulent domain. This figure is constructed from a period of observations using  $\Phi_{\parallel} = -\int E_{\parallel} v_{\text{struc}} dt$ , where  $E_{\parallel}$  is measured and  $v_{\text{struc}} = 2000 \text{ km s}^{-1}$  is the structure speed (the [companion paper](#)). Over the 18 minute turbulent period in the observations,  $\Phi_{\parallel}$  has a standard deviation of  $\sim 200 \text{ V}$ .

As an electron propagates, there is a  $\sim 50\%$  probability of encountering an accelerating  $\Delta\Phi_{\parallel}$  (energy gain) and a 50% probability of encountering a decelerating  $\Delta\Phi_{\parallel}$ . An encounter with decelerating  $\Delta\Phi_{\parallel}$  has two possible outcomes: (a) loss of energy or (b) reflection if  $W_{e\parallel} < q\Delta\Phi_{\parallel}$  ( $q$  is charge). Electrons entering the turbulent region with low  $W_{e\parallel}$  have a higher probability of reflection than do those with high  $W_{e\parallel}$ . As a result, relatively few low- $W_{e\parallel}$  electrons enter the turbulent region, as seen in Figure 2(a) and as depicted in Figure 2(h).

Inside of the turbulent region, the remaining low- $W_{e\parallel}$  electrons are energized. While an electron gains energy on all encounters with accelerating  $\Delta\Phi_{\parallel}$ , it loses energy during an encounter with a decelerating  $\Delta\Phi_{\parallel}$  only if it is not reflected (ignoring structure velocity). Therefore, low- $W_{e\parallel}$  electrons, which experience more reflections, gain energy. In steady state (after 5–10 s), the number of low- $W_{e\parallel}$  electrons is dramatically reduced, so  $T_{e\parallel}$  remains elevated with little parallel energization. High- $W_{e\parallel}$  electrons freely pass through the turbulence with little parallel energization since  $\sum \Delta\Phi_{\parallel} \approx 0$  unless there is a net  $\Phi_{\parallel}$ . Given that the observed turbulence endures for  $\sim 18$  minutes and that, in the simulation, few of the original (preloaded) electrons remain after  $\sim 10$  s, one can see that an open-boundary simulation is critical.

The electron distributions (Figures 2(f) and (g)) show a clearer picture. When averaged over all pitch angles, the distribution inside of the simulation domain indicates heating to an average  $T_e \sim 5 \text{ keV}$ , which compares remarkably well to the measured values ( $T_e \sim 4.7 \text{ keV}$ ). However, when separated by pitch angle, a parallel electron distribution,  $f(p_{\parallel})$  shows a clearly visible “shoulder” at  $\sim 3$  to  $\sim 5 \text{ keV}$ . A similar “shoulder” or “flat-top” distribution is seen in the observations (e.g., Figures 4(k) and 5(l) in the [companion paper](#)).

A net  $\Phi_{\parallel}$  at the boundaries of the turbulent region that accelerates electrons into the turbulent region also could produce the observed electron distributions (e.g., Newman et al. 2001; Andersson et al. 2002; Egedal et al. 2015). A large net  $\Phi_{\parallel}$  combined with strong wave activity often results in a “flat-top”  $f(p_{\parallel})$  with increased  $T_{e\parallel}$  and decreased  $n_e$ . A net  $\Phi_{\parallel}$  cannot be ruled out via the  $E_{\parallel}$  measurement given the  $\pm 1 \text{ mV m}^{-1}$  uncertainty. However, observations at the boundaries indicate low  $\langle \mathbf{J} \cdot \mathbf{E} \rangle_{\parallel}$  and almost no change in electron pressure (not shown), so a net  $\Phi_{\parallel}$  is unlikely. Furthermore, the test-particle simulation indicates that a net  $\Phi_{\parallel}$  is not required.

The defined  $d_{\text{corr}}$  also has some noteworthy consequences in perpendicular energization. The first adiabatic moment ( $\mu$ ) is conserved unless the electrons experience changes in  $\mathbf{E}_{ac\perp}$  that occur on timescales  $\delta t < 1/f_{ce}$ , where  $f_{ce}$  is the electron cyclotron frequency. At first glance, perpendicular energization should be minor since  $\mathbf{E}_{ac}$  power at  $f \geq f_{ce}$  is small in the rest frame (Figure 3(d) of the [companion paper](#),  $f_{ce} \sim 550 \text{ Hz}$ ). However, electrons with high parallel speeds ( $v_{e\parallel} > d_{\text{corr}} f_{ce}$ ) traverse  $d_{\text{corr}}$  in less time than  $1/f_{ce}$  and therefore experience changes in  $\mathbf{E}_{ac\perp}$  faster than  $1/f_{ce}$ , which can change  $\mu$ . In other words, in its ( $v_{e\parallel}$  motion) frame, an electron sees higher power in  $\mathbf{E}_{ac\perp}$  at  $f \geq f_{ce}$  via Doppler shift ( $\delta f \sim v_{e\parallel}/d_{\text{corr}}$ ). Interestingly, the electron thermal

velocity in the turbulent region is roughly the same as  $d_{\text{corr}} f_{ce}$ . The simulation supports this interesting relation between  $T_{e\parallel}$  and the perpendicular heating rate.  $\langle \mathbf{J} \cdot \mathbf{E} \rangle_{\perp}$  increases with increasing  $T_{e\parallel}$  (not shown).

A number of simulations have been executed with different initiations and changes in  $d_{\text{corr}}$ ,  $t_{\text{corr}}$ , and the PDF of  $\mathbf{E}_{ac}$ . In summary, changing initiation (preloading of  $n_e$  and  $T_e$ ) without changing the boundary conditions produces the same (within expected variations) final quasi-equilibrium state after  $\sim 5$  to  $\sim 10$  s. Changing  $d_{\text{corr}}$  has a significant influence on energization. Smaller  $d_{\text{corr}}$  results in lower  $T_{e\parallel}$  with an increase in  $T_{e\perp}$ . Larger  $d_{\text{corr}}$  results in higher  $T_{e\parallel}$  with a minor decrease in  $T_{e\perp}$ . As expected, altering  $t_{\text{corr}}$  by up to a factor of 2 does not significantly alter the results. Energization increases with increasing  $\langle |\mathbf{E}_{ac}|^2 \rangle$ . However, we find that the shape of the PDF of  $\mathbf{E}_{ac}$  has a smaller impact on the results as long as  $\langle |\mathbf{E}_{ac}|^2 \rangle$  is not altered.

As a final note, energization also can be increased by gyromotion if  $\rho_e \geq d_{\text{corr}}$ , where  $\rho_e$  is the electron gyroradius. However, if  $\rho_e \geq d_{\text{corr}}$ , then  $W_{e\perp} \geq 70 \text{ keV}$ , so such energization acts only on high-energy electrons. This effect, however, cannot be studied with 1D test-particle simulations.

### 3.2. Electron Test-particle Simulations with a Time-stationary Depletion in $\mathbf{B}(\mathbf{x})$

With  $\mathbf{B}$  constant, the electron distributions in the simulation show little if any development of a nonthermal tail (Figures 2(f) and (g)), whereas the observed electron distributions show significant acceleration (the [companion paper](#)). Since the observations indicate that trapping plays a prominent role, the simulation is repeated with a time-stationary  $\mathbf{B}$  depletion in the center of the domain (Figures 3(a) and (b)). In this simulation, the mirror force is active (see the [Appendix](#)).

Run 1 ( $\mathbf{B}$  constant) and Run 2 (time-stationary  $\mathbf{B}$  depletion) have many similarities. There is a rapid rise in  $T_{e\parallel}$  (in both space and time) and an  $n_e$  depletion at the boundaries of the turbulent region (Figures 3(c)–(e)). The thermal core of the average distribution ( $f_{\text{ave}}$ ) in Run 2 (Figure 3(f)) is heated to roughly the same temperature as in Run 1. A shoulder appears in  $f(p_{\parallel})$  while the perpendicular heating is initially slow (Figure 3(g)).

A marked difference in Run 2 is that  $T_{e\perp}$  (Figure 3(c)) is considerably higher in the  $\mathbf{B}$  depletion and continues to rise for the duration of the run (Figure 3(e)). The density is also increased in the  $\mathbf{B}$  depletion (Figure 3(d)) due to trapping. Electrons that enter the  $\mathbf{B}$  depletion and experience sufficient perpendicular energization continuously add to the trapped population. Since perpendicular energization is much higher than parallel energization, once trapped, relatively few electrons escape. The result is near runaway nonthermal acceleration. Interestingly, the added electron pressure could serve to deepen the magnetic depletion in a self-consistent treatment.

Another important difference in Run 2 is the development of a significant nonthermal tail (compare Figures 3(f) and (g) with Figures 2(f) and (g)) that is primarily in  $f(p_{\perp})$  between 30 and  $\sim 250 \text{ keV}$ . Figure 3(h), which plots the normalized phase-space density as a function of pitch angle and distance for 75–125 keV electrons, shows that accelerated particles are predominantly trapped inside of the  $\mathbf{B}$  depletion. These electron distributions are, again, remarkably similar to those

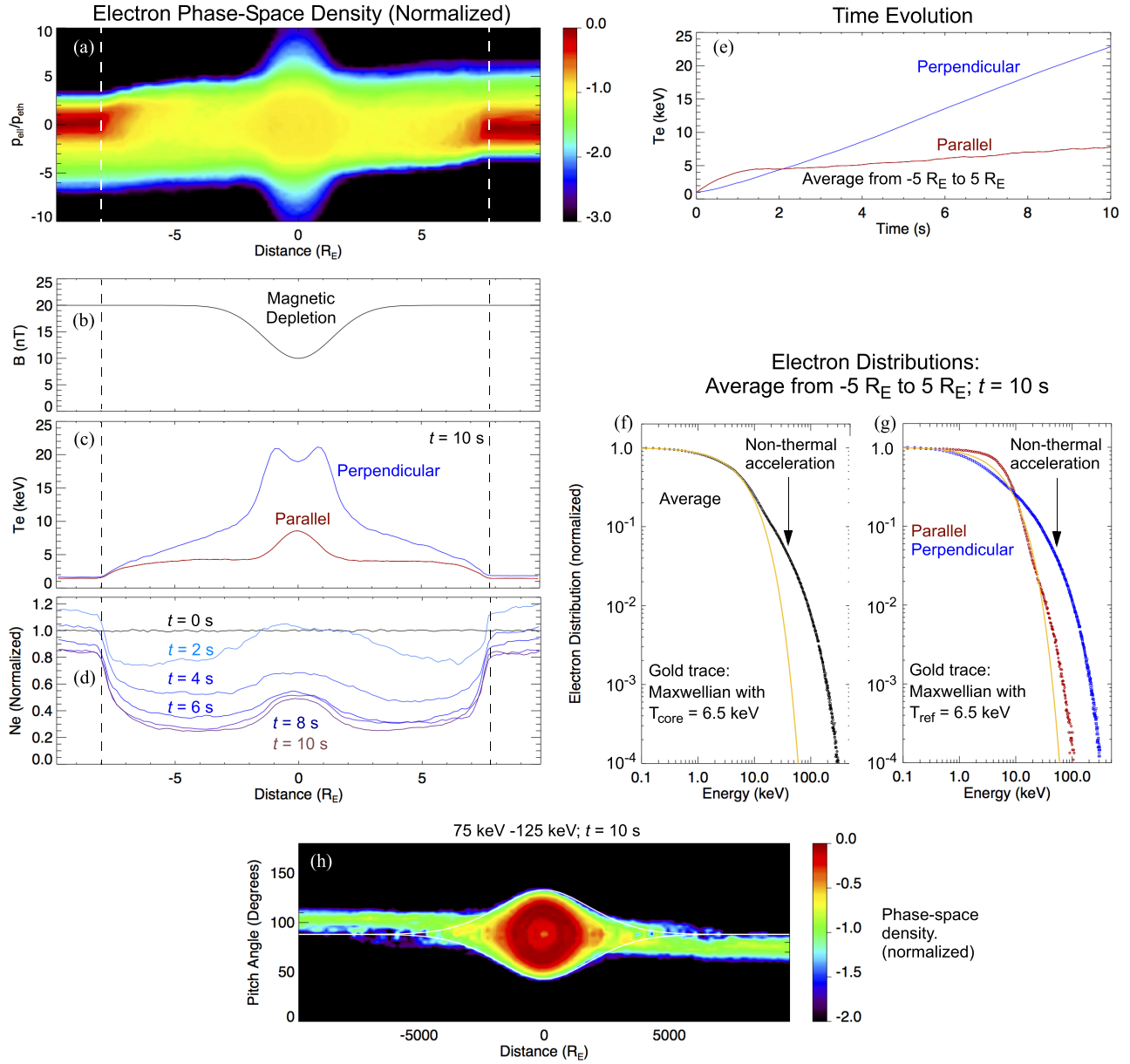


**Figure 3.** A test-particle simulation with a magnetic depletion. (a) The phase-space density at  $t = 10$  s. (b)  $B$ . (c)  $T_{e\parallel}$  and  $T_{e\perp}$ . (d) Density. The colors represent time. (e)  $T_{e\parallel}$  and  $T_{e\perp}$  as a function of time. (f) and (g) The electron distribution. The black trace is averaged over all directions, the blue trace is  $f(p_{\perp})$ , the red trace is  $f(p_{\parallel})$ , and the gold trace is a Maxwellian distribution with  $T_e = 6.1$  keV. (h) The phase-space density of 75–125 keV electrons as a function of pitch angle. The white traces indicate trapping boundaries. Energized electrons are primarily trapped.

observed (Figures 4(h)–(j) and 5(f)–(h) in the [companion paper](#)).

In short, the test-particle simulations reproduce many of the observed characteristics of the observed electron energization both qualitatively and quantitatively. The low-energy thermal cores in the turbulent region appear to have  $T_{e\parallel} > T_{e\perp}$ . An abrupt depletion of  $n_e$  appears at the boundaries of the turbulent region. A “shoulder” or “flat-top” distribution is seen in  $f(v_{\parallel})$ . A significant nonthermal tail develops in the trapped distribution inside of the  $B$  depletions.

As discussed earlier, perpendicular energization increases with increasing  $v_{e\parallel}$ . If  $v_{e\parallel} > d_{\text{corr}} f_{ce}$ , the first adiabatic invariant ( $\mu$ ) is no longer conserved. As such, perpendicular energization is stronger inside of a  $B$  depletion as two phenomena conspire. Electrons enter the  $B$  depletion and thus travel into a weaker  $B$ , so  $v_{e\parallel}$  increases. At the same time,  $f_{ce}$  decreases. These two

changes combine to break  $\mu$  for the majority of electrons inside of the  $B$  depletion.

### 3.3. Electron Test-particle Simulations with a Time-varying Depletions in $B$

The test-particle simulations indicate near runaway acceleration inside of a time-stationary  $B$  depletion. Clearly, the lifetime of a  $B$  depletion may limit or control acceleration. As an experiment, we introduce two types of simple time variations in  $B$  that endure for  $\sim 5$  s. We cannot directly measure lifetimes of  $B$  depletions, but they are constrained by observations to be greater than several seconds. One way to develop (then collapse) a  $B$  depletion is to allow  $B$  to decrease (then increase) keeping the length along  $B$  constant (Figure 4(a)). Since  $\mu$  is conserved under slow changes in  $B$ , this case should generate betatron

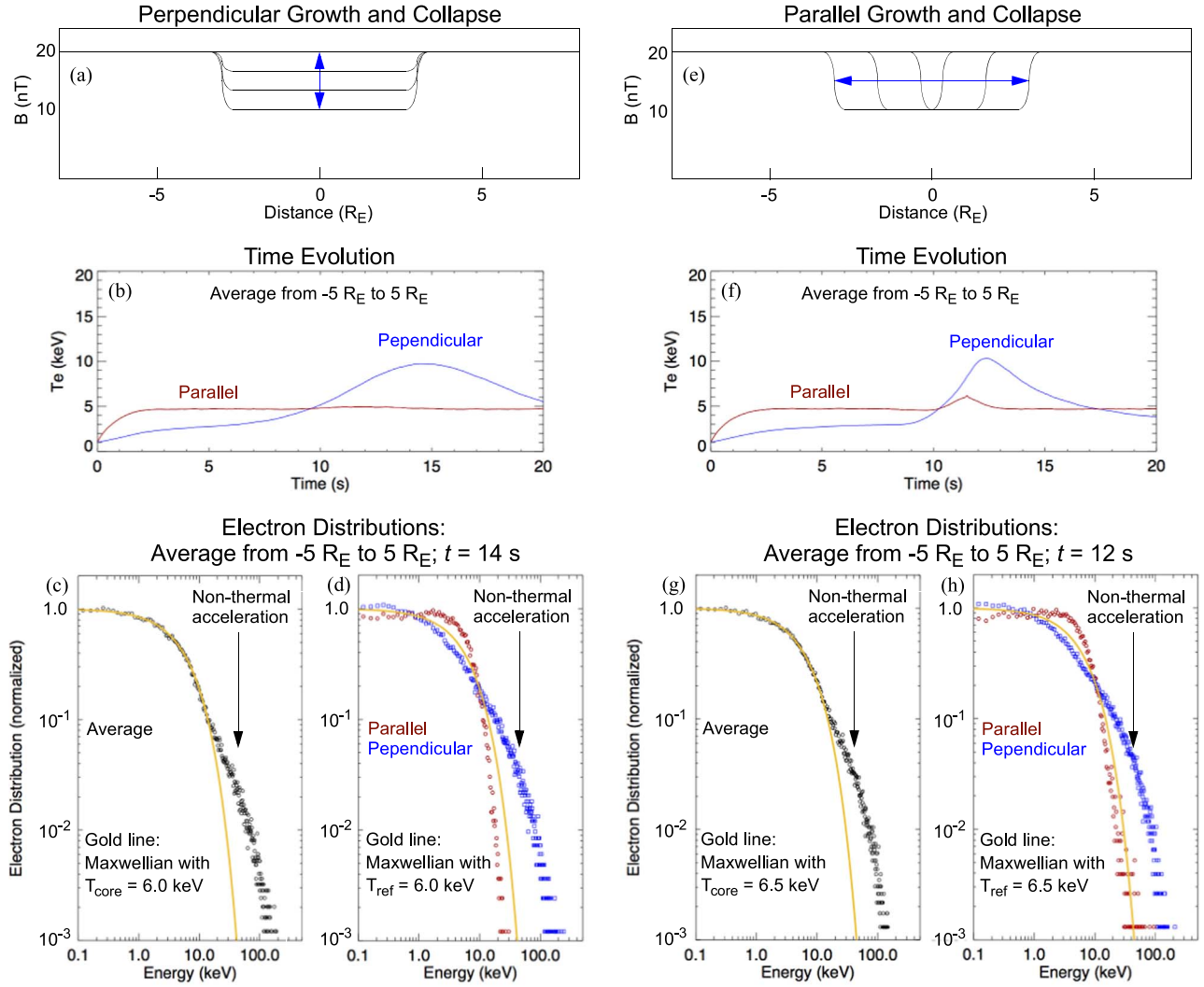


**Figure 4.** Test-particle simulations with time-varying depletions in  $B$ . (a) A cartoon of a betatron-like  $B$  depletion (constant spatial profile).  $B$  is constant until  $\sim 5$  s and begins depleting. It recovers at  $\sim 15$  s. The time profile is Gaussian. (b)  $T_{e\parallel}$  and  $T_{e\perp}$  as a function of time averaged over 25 runs (see the [Appendix](#)). (c) and (d) The electron distribution. The black trace is averaged over all directions, the blue trace is  $f(v_{e\perp})$ , the red trace is  $f(v_{e\parallel})$ , and the gold trace is a Maxwellian distribution with  $T_e = 6.0$  keV. (e) A cartoon of a Fermi-like  $B$  depletion (diverging then converging mirrors), (f)  $T_{e\parallel}$  and  $T_{e\perp}$  as a function of time.  $T_{e\parallel}$  increases as the mirrors collapse. (g) and (h) The electron distribution. The gold trace is a Maxwellian distribution with  $T_e = 6.5$  keV.

cooling then heating in addition to the energization from  $E_{ac}$ . Another method is to have the  $B$  depletion grow then collapse by expanding then contracting along  $B$  (Figure 4(e)). The expansion and contraction activates Fermi-like parallel cooling (then acceleration) by moving magnetic mirrors.

The results in Figure 4 are an average of a set of simulations that are initiated with lower densities ( $\sim 40\%$  of nominal) and fewer particles than those in Figures 1 and 2. Averaging over multiple simulation runs highlights the behavior of  $T_{e\parallel}$  and  $T_{e\perp}$ . Details are in the [Appendix](#).

Figure 4(b) shows the time histories of  $T_{e\parallel}$  and  $T_{e\perp}$  over 20 s with a  $B$  depletion undergoing perpendicular (betatron) development then collapse (Figure 4(a)). The  $B$  depletion develops between 5 to 10 s and collapses between 10 and 15 s with a Gaussian time profile. For the first  $\sim 5$  s,  $T_{e\parallel}$  and  $T_{e\perp}$  behave as in the time-stationary simulation (Figure 2) and approach the quasi-equilibrium state. Betatron (adiabatic) cooling prior to 8 s as  $B$  depletes is not apparent since it is offset by perpendicular electron energization by  $E_{ac}$ . There are few trapped electrons before  $\sim 8$  s. As the  $B$  depletion deepens, perpendicular energization of trapped electrons overcomes

adiabatic cooling so  $T_{e\perp}$  rises prior to 10 s. After 10 s, betatron energization and perpendicular energization combine.  $T_{e\perp}$  rises and then peaks at  $\sim 14$  s, displaying a significant nonthermal tail (Figures 4(c) and (d)). After 15 s, the system relaxes toward quasi-equilibrium.

Figure 4(f) shows the time histories of  $T_{e\parallel}$  and  $T_{e\perp}$  over 20 seconds with a  $B$  depletion under parallel development and collapse (Figure 4(e)). As in the previous case, the  $B$  depletion develops between 5 s to 10 s and collapses between 10 and 15 s.  $T_{e\parallel}$  and  $T_{e\perp}$  behave as expected for the first 5 s. In this case, there is a very small drop in  $T_{e\parallel}$  between 8 and 9.5 s as the diverging magnetic mirrors cool the plasma in a Fermi-like fashion.  $T_{e\perp}$  rises prior to 10 s as trapped particles are energized by  $E_{ac}$ . As the  $B$  depletion collapses, one can see significant differences between the betatron and Fermi-like collapse. In the Fermi-like collapse,  $T_{e\parallel}$  and  $T_{e\perp}$  both rise. The rise in  $T_{e\parallel}$  is expected from Fermi acceleration of collapsing mirrors. However, the rise in  $T_{e\parallel}$  is limited by the rapid loss of high  $v_{e\parallel}$  electrons from the simulation domain. The sharp rise in  $T_{e\perp}$  is due in part from ongoing perpendicular energization and in

part from parallel energy converting to perpendicular energy in the mirroring regions. Interestingly,  $T_{e\perp}$  rapidly lowers after the  $\mathbf{B}$  depletion collapses due to rapid transport out of the system.

### 3.4. Summary of Electron Energization

Particle trapping in time-varying  $\mathbf{B}$  depletions undoubtedly influences electron energization, but we caution that we have examined only two specific time-varying cases with test-particle simulations that are not self-consistent. A large parameter space remains unexplored.

There are, however, several concrete conclusions on electron energization that one can derive from the analysis of observations (the [companion paper](#)) and test-particle simulations. Turbulence generates both the intense  $\mathbf{E}_{ac}$  and the depletions in  $\mathbf{B}$ .  $\mathbf{E}_{ac}$  has a modest parallel energization rate, but creates a rapid rise (in distance and time) in the thermal core  $T_{e\parallel}$  due to what is primarily a “ $\Delta\Phi_{\parallel}$  filter” effect. Low  $W_{e\parallel}$  electrons entering the turbulent region have a high probability of reflection, whereas high  $W_{e\parallel}$  electrons can penetrate into the turbulent region.

The defined correlation distance ( $d_{\text{corr}}$ ) in  $\mathbf{E}_{ac}$  ( $f > f_{ci}$ ) favors perpendicular energization for electrons with high  $v_{e\parallel}$ . A simple explanation is that electrons with high  $v_{e\parallel}$  traverse  $d_{\text{corr}}$  in less than a gyro-period, which breaks  $\mu$ . Another view is that, in its ( $v_{e\parallel}$  motion) frame, a high  $v_{e\parallel}$  electron experiences a Doppler-shifted  $\mathbf{E}_{ac}$  spectrum with stronger power at  $f_{ce}$ . Furthermore, at higher  $W_{e\perp}$  ( $\sim 70$  keV),  $\rho_e$  can exceed  $d_{\text{corr}}$ , which can increase energization (this latter effect is not reproduced in a 1D simulation). Basically, turbulence creates a heating mechanism that favors high-energy particles. Such heating mechanisms produce nonthermal distributions.

A principal conclusion is that particle trapping in  $\mathbf{B}$  depletions plays a chief role in the development of a nonthermal tail. The observations have many cases of energetic electrons within trapping boundaries. The role of trapping is reinforced by test-particle simulations. A time-stationary  $\mathbf{B}$  depletion leads to near runaway acceleration.

The finite lifetimes of  $\mathbf{B}$  depletions appear to be a limiting factor to acceleration but also may explain the differences that one sees in observed electron distributions. The two cases of development and collapse of magnetic depletions, betatron and Fermi-like, have different energization profiles, particularly in  $T_{e\parallel}$ . Interestingly, the two processes, betatron acceleration and Fermi-like acceleration maintain nearly the same ratio of the total energy to the magnetic field amplitude  $W_e/|\mathbf{B}|$ , so they are difficult to distinguish in the observations. Magnetic pumping is well established as a mechanism to amplify heating and may be active in turbulent plasmas.

## 4. Ion Energization

The ion fluxes observed in the large-scale turbulent region have different characteristics than do the electron fluxes (the [companion paper](#)). While electron fluxes appear in short bursts (several seconds), ion fluxes vary on longer timescales. Ions have much higher thermal core temperatures as well as a significant nonthermal tail with a power-law index  $\sim -3$ .

One expects a considerably different energization process for ions than for electrons. Ions have significantly larger gyroradii and can directly draw energy from DC  $\mathbf{E}$  via quasi-adiabatic or chaotic orbits in the reversing magnetic field (Speiser 1965). Equally, if not more importantly, turbulence causes a cascade

of energy through the inertial region to the dissipation scale at  $k\rho_i \sim 1$  ( $f \sim f_{ci}$ ). Basically, turbulence channels energy to  $k\rho_i \sim 1$  and  $f \sim f_{ci}$  where ions can experience direct cyclotron- or gyro-resonant energization.

### 4.1. Analytic Analysis

The classical (nonrelativistic) cyclotron energization rate from plasma waves is well established (Chang et al. 1986):

$$\dot{W}_i = \frac{e^2}{2m_i} \eta_L P_E(f_{ci}) \quad (2)$$

where  $e$  is the fundamental charge,  $m_i$  is the ion mass,  $P_E$  is the power spectral density (PSD) of  $\mathbf{E}$ , and  $\eta_L$  (estimated to be 1/2) is the fraction of  $P_E$  that is left-hand polarized. In the observations,  $P_E(f_{ci}) \sim 10^{-4} \text{ V m}^{-2} \text{ Hz}^{-1}$  (Figure 3(d) in the [companion paper](#)), which implies that  $\dot{W}_i = 2.4 \text{ keV s}^{-1}$  per ion. This perpendicular energization mechanism could dominate and, when combined with the energy from DC  $\mathbf{E}$ , is consistent with the measured  $\langle \mathbf{J} \cdot \mathbf{E} \rangle_{\text{Tot}} / \langle n \rangle$  in Table 1.

A less likely possibility is that the ions experience random heating from  $\mathbf{E}_{ac}$  ( $f > f_{ci}$ ). Unlike electrons, most ions do not traverse  $d_{\text{corr}}$  in less time than  $t_{\text{corr}}$ , so temporal changes in  $\mathbf{E}_{ac}$  are dominant. An individual ion undergoes a series of uncorrelated impulses,

$$\delta \mathbf{p} = e \mathbf{E}_{ac} t_{\text{corr}}, \quad (3)$$

that result in a “random walk” in momentum. During an impulse, the energy change is:

$$\begin{aligned} \delta W_i^2 &= [(\mathbf{p}_o + \delta \mathbf{p})c]^2 + (m_i c^2)^2 - [\mathbf{p}_o c]^2 + (m_i c^2)^2 \\ &= [2\mathbf{p}_o \cdot \delta \mathbf{p} + \delta \mathbf{p}^2] c^2 \end{aligned} \quad (4)$$

where  $\mathbf{p}_o$  is the momentum prior to an impulse. In second order heating, the impulse has a random direction and sign compared to the initial velocity, so the net energy change after  $N$  impulses is:

$$\sum_N \delta W_i^2 \approx N \langle \delta \mathbf{p}^2 \rangle c^2 = e^2 t_{\text{corr}}^2 N \langle |\mathbf{E}_{ac}|^2 \rangle c^2. \quad (5)$$

The resulting heating rate after a time period of  $N t_{\text{corr}}$  is then:

$$2W_{iR} \dot{W}_i \approx \frac{e^2 c^2 t_{\text{corr}}^2 N \langle |\mathbf{E}_{ac}|^2 \rangle}{N t_c} \quad (6)$$

$$\dot{W}_{iR} \approx \frac{e^2 t_{\text{corr}} \langle |\mathbf{E}_{ac}|^2 \rangle}{2W_{iR}/c^2}. \quad (7)$$

Here,  $W_{iR}$  includes the rest energy. Using  $t_{\text{corr}} = 24 \text{ ms}$  and the measured  $\langle |\mathbf{E}_{ac}|^2 \rangle$ , the second order heating rate is  $\sim 0.2 \text{ keV s}^{-1}$ . This value is significantly less than the cyclotron-resonant heating.

### 4.2. Ion Test-particle Simulation with Direct Application of Measured $\mathbf{E}$ and $\mathbf{B}$

The analytic exercise reinforces much of the expected energy transfer in turbulent plasmas (e.g., Matthaeus et al. 1984). The primary energy transfer into ions occurs at scales of  $\rho_i$  or at

frequencies near  $f_{ci}$ . This energy is continuously replenished via a cascade process.

There is a simple test that one can perform to verify the dominance of cyclotron- or gyro-resonant energization. Since ion velocities are less than or similar to the characteristic velocity ( $\sim 2000 \text{ km s}^{-1}$ ) of the  $\mathbf{E}$  structures (the [companion paper](#)), we can directly apply measured  $\mathbf{E}$  and  $\mathbf{B}$  time series to a set of test particles. The size of the turbulent region is roughly  $10^5 \text{ km}$  and the average ion velocity is about  $2000 \text{ km s}^{-1}$  (20 keV), so ions are expected to dwell in the turbulent region for roughly one minute. The observed turbulence endures for  $\sim 18$  minutes so, for each test particle, we select a random one-minute section of the vector  $\mathbf{E}$  and  $\mathbf{B}$  measurements.

Figure 5(a) displays the results of 100,000 test particles (ions) that are initiated as a thermal distribution ( $T_i = 4 \text{ keV}$ ) then exposed to random (different for each ion) one-minute sections of the measured  $\mathbf{E}$  and  $\mathbf{B}$ .  $\mathbf{E}$  is low-pass filtered to  $\sim 50 \text{ Hz}$  so that it can be interpolated to match the time cadence of  $\mathbf{B}$ . Very little ion heating is expected at frequencies above 50 Hz. The test particles are advanced via the Lorentz force,  $d\mathbf{p}/dt = e(\mathbf{E} + \mathbf{v} \times \mathbf{B})$ . Ions experience  $\mathbf{E}$  and  $\mathbf{B}$  for the entire one-minute period; they do not exit the turbulent region. Therefore, this particular simulation reveals an energization rate rather than a realistic temperature profile inside of a finite-sized domain. The black trace follows the average energy of the ions. To avoid a large “pick-up” energy at the start of the simulation from DC  $\mathbf{E}$ ,  $\mathbf{E}$  starts at zero and is slowly ramped for 4 s (one half of an ion gyro-period). The black trace suggests an energization rate of  $3.0 \text{ keV s}^{-1}$  per ion, which is in consort with cyclotron energization rate. To generate the blue trace, we apply the measured  $\mathbf{E}_{ac}$  ( $\mathbf{E}$  filtered to  $f > 0.25 \text{ Hz}$ ). The filtering removes most, but not all, of the power near  $f_{ci}$ . The energization rate ( $370 \text{ eV s}^{-1}$ ) is dramatically lower. Interestingly, if  $\mathbf{E}$  is filtered to  $f > 0.5 \text{ Hz}$  (red trace), the energization rate is near negligible. The direct application of measured  $\mathbf{E}$  and  $\mathbf{B}$  to test particles, while not fully justified, corroborates that DC  $\mathbf{E}$  and cyclotron- or gyro-resonant energization are dominant.

#### 4.3. Ion Test-particle Simulations in a Finite Domain

A finite domain size has a significant influence on ion energization. Ions enter then exit the region of turbulence on the order of one minute whereas the duration of the turbulence is  $\sim 18$  minutes, so the above test cannot realistically reproduce a measured ion distribution. To do so, we repeat the test-particle simulations using a similar code as used for electrons. However, there are several major changes that are required to treat ions properly. Since  $\rho_i$  is many times the correlation length scale of  $\mathbf{B}$ , ions experience significant fluctuations ( $\delta\mathbf{B}$ ) as they orbit, which can cause substantial pitch-angle diffusion. To include this effect,  $\delta\mathbf{B}$  is imposed along an ion orbit maintaining 20 nT background field.

Another significant change is that  $\mathbf{E}$  must include power at  $f \sim f_{ci}$ . Unfortunately,  $d_{\text{corr}}$ ,  $t_{\text{corr}}$  and the PDF are not well defined for low-frequency  $\mathbf{E}$ , so the low-frequency  $\mathbf{E}$  is implemented as a set of randomly phased waves that reproduce the observed spectrum. The implementation  $\mathbf{E}$  and  $\delta\mathbf{B}$  are described further in the [Appendix](#).

Even with the above changes, a 1D test-particle simulation is limited. A DC  $\mathbf{E}$  should be considered. Ions can drift through the magnetotail (primarily) in the  $Y$  direction with quasi-adiabatic or chaotic orbits in the reversing magnetic field

(Speiser 1965). If so, they gain energy, which depends on the DC value of  $E_y$  and the extent of the reconnection region in  $Y$ . To examine such energization, a 3D simulation is required. Such a simulation is a subject of a future study.

The 1D simulation domain is depicted in Figure 5(b). We begin with background  $\mathbf{B}$  fixed at +20 nT. Ion distributions at the  $\pm X$  boundaries have a source temperature of 4 keV and a normalized density of 1.  $\mathbf{E}$ ,  $\mathbf{B}$ , and  $\delta\mathbf{B}$  are imposed as described in the [Appendix](#).

Figures 5(c)–(f) display, in order, the normalized ion phase-space density at  $t = 300 \text{ s}$ ,  $T_{i\parallel}$  and  $T_{i\perp}$  as a function of distance, density as a function of distance (colors represent time), and the time evolution of  $T_{i\parallel}$  and  $T_{i\perp}$ . These plots suggest that ion behavior is qualitatively similar to that of electrons, albeit on differing time and energy scales. Electrons reach a quasi-equilibrium state in  $\sim 10 \text{ s}$  whereas ions take over a 100 s. The density depletions and high temperatures in the turbulent region for electrons and ions are similar (compare Figures 5(d) and (e) to Figures 2(c) and (d)).

However, the  $n_i$  depletion is caused by a different process. Ions experience strong perpendicular energization and are scattered by  $\delta\mathbf{B}$ , which transfers perpendicular energy to parallel energy. High  $T_{i\parallel}$  then causes transport out of the turbulent region. The parallel distribution function of the ions (Figure 5(g)) does not show a dramatic flat-top that is seen in the electron distributions.

Ion energization is dominated by cyclotron resonance. The quasi-equilibrium state has  $T_{i\perp} \sim 51 \text{ keV}$  and  $T_{i\parallel} \sim 30 \text{ keV}$ , with an average  $T_i \sim 43 \text{ keV}$  (Figures 5(f) and (g)). These quasi-equilibrium values are more than a factor of two higher than supported by observations, even though energization via DC  $E_y$  is not included in the simulation. There are several plausible explanations for this discrepancy. The physical size of the turbulent region is roughly estimated and a smaller parallel size would lead to lower  $T_i$ . Unlike electrons, a significant flux of ions could enter and exit the  $Z$  and  $Y$  boundaries of the turbulent region, which could influence  $T_i$ . Finally, self-consistent waves may have different energization properties.

Figure 5(h) shows the sensitivity of the quasi-equilibrium  $T_{i\parallel}$  and  $T_{i\perp}$  to the rms amplitude of  $\mathbf{E}$ . The spectral shape of  $\mathbf{E}$  is not changed as its amplitude is varied.  $\delta\mathbf{B}$  and  $\mathbf{B}$  are fixed. These simulations are run for 500 s, which is needed to reach a quasi-equilibrium state at low values of  $E_{\text{rms}}$ . Figure 5(h) demonstrates the influence of the finite domain size. A quadratic increase of  $T_{i\parallel}$  and  $T_{i\perp}$  with  $E_{\text{rms}}$  is expected ( $E_{\text{rms}}^2$ —gold trace) in an infinite domain. However, as  $T_{i\parallel}$  rises, ions experience a shorter dwell time in the turbulent region which limits energization.

Figure 5(i) displays the impact of  $\delta\mathbf{B}$ .  $\mathbf{B}$  and  $\mathbf{E}$  fixed. The most noticeable feature is that, with  $\delta\mathbf{B} = 0$ ,  $T_{i\perp}$  exceeds 200 keV, whereas  $T_{i\parallel}$  has but a minimal rise. With little scattering from  $\delta\mathbf{B}$ ,  $T_{i\parallel}$  remains low, so ions have long dwell times in the turbulent region. As such, the strong perpendicular energization causes the substantial rise in  $T_{i\perp}$ . However, if scattering due to  $\delta\mathbf{B}$  is increased,  $T_{i\parallel}$  is increased, so ions exit the simulation domain more rapidly. Ironically, parallel energization acts to limit the increase in  $T_{i\perp}$  in a finite domain.

To investigate the effect of magnetic depletions,  $\mathbf{B}$  depletions are imposed in the center of the turbulent region. Figure 5(j) displays the imposed  $\mathbf{B}$  depletions of 0 (black), 5 nT (blue), 10 nT (green), and 15 nT (red). Figure 5(k) displays the normalized distribution functions that result from each of the

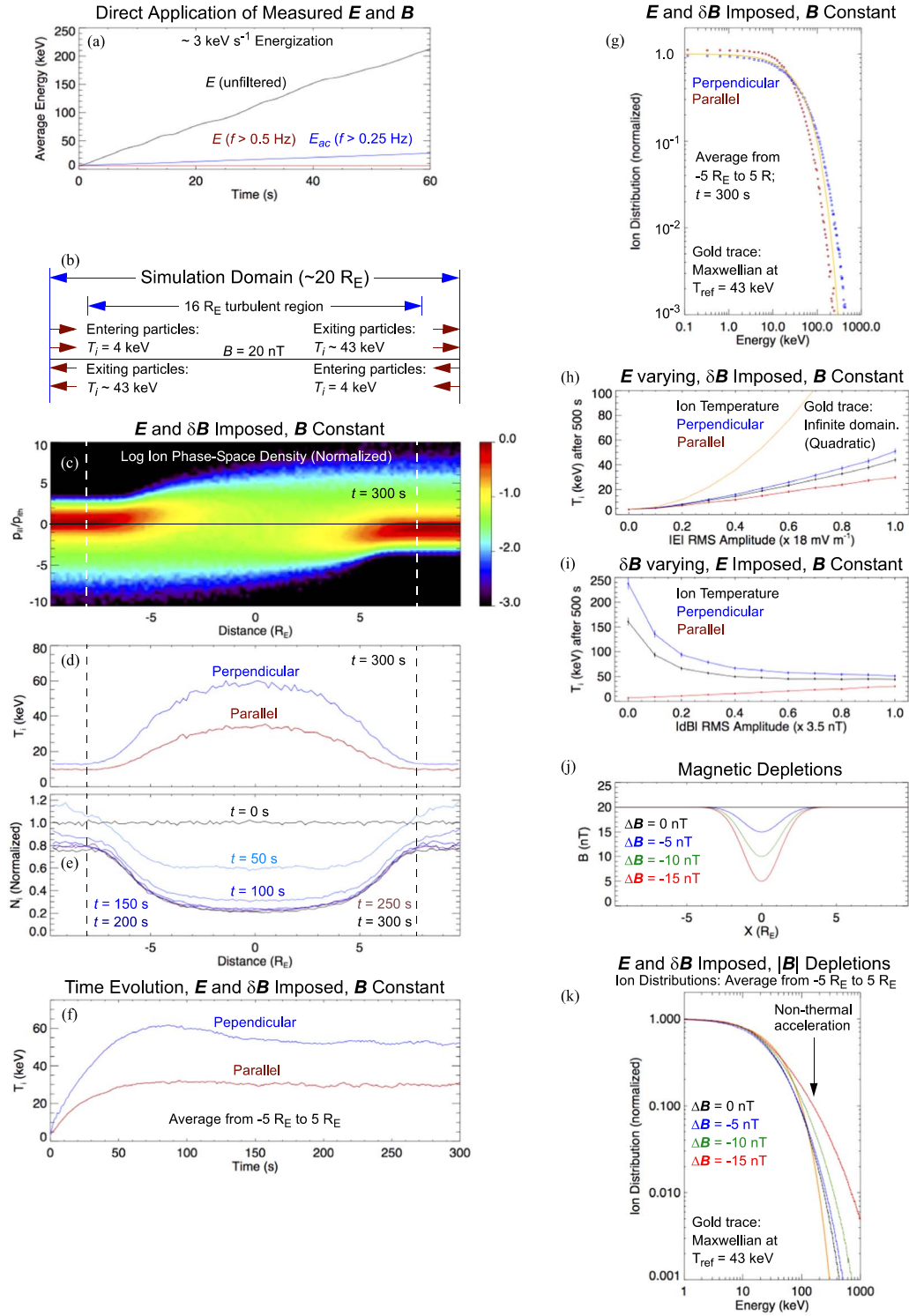


**Figure 5.** Test-particle simulations of ion energization. (a) Ion energization under a direct application of measured  $E$  and  $B$ . With  $E$  unfiltered (black trace), energization is  $\sim 3 \text{ keV s}^{-1}$  per particle. If power at  $f_{ci}$  is removed (blue and red traces), the energization is greatly reduced. (b) A 1D spatial, 3D velocity, open boundary test-particle simulation of ion energization.  $B$  is constant at  $+20 \text{ nT}$ .  $\delta B$  and  $E$  are imposed (see the Appendix). The simulation domain extends approximately  $\pm 10 R_E$ . Inside of the simulation domain, the turbulent region extends  $\pm 8 R_E$  ( $10^8 \text{ m}$ ), marked by vertical dashed lines. It is initiated with  $T_i = 4 \text{ keV}$  and a normalized density of 1, which is the ion population imposed at the two boundaries. (c) The normalized ion phase-space density at  $t = 300 \text{ s}$ . The raw image is 125 pixels in distance and 50 pixels in  $p_{\parallel}$  and smoothed to higher resolution. (d)  $T_{i\perp}$  and  $T_{i\parallel}$  as a function of distance at  $300 \text{ s}$ . (e) The density as a function of distance. The colors represent time. (f)  $T_{i\perp}$  and  $T_{i\parallel}$  as a function of time with  $B$  constant. The quasi-equilibrium temperatures are about twice that observed. (g) The normalized ion distribution as a function of energy. The blue trace is  $f(p_{i\perp})$ , the red trace is  $f(p_{i\parallel})$ , and the gold trace is a Maxwellian distribution with  $T_i = 43 \text{ keV}$ . There is significant heating but little acceleration. (h) The quasi-equilibrium  $T_{i\perp}$  and  $T_{i\parallel}$  as a function of  $E_{\text{rms}}$ . The gold trace is a quadratic response that is expected in an infinite domain. (i) Quasi-equilibrium  $T_{i\perp}$  and  $T_{i\parallel}$  as a function of  $\delta B_{\text{rms}}$ . (j) The imposed depletions in  $B$ . (k) Ion distribution averaged over all angles. The colors correspond to depletion in  $B$  in panel (j). The gold trace is a  $43 \text{ keV}$  Maxwellian distribution for visual reference.

magnetic depletions. The effect of the magnetic depletions is primarily to enhance the acceleration tail of the ion distribution. A depletion of 15 nT (red trace in Figures 5(i) and (k)) disproportionately enhances the accelerated ions over the milder depletions. Apparently, the scattering due to  $\delta\mathbf{B}$  limits ion trapping in low-amplitude depletions, so a deep depletion is required to significantly enhance acceleration.

#### 4.4. Summary of Ion Energization

The solid conclusion from the above analysis is that ion energization is primarily from the power in  $\mathbf{E}$  with  $f \sim f_{ci}$  or  $k\rho_i \sim 1$ , which leads to perpendicular heating. Scattering  $\delta\mathbf{B}$  acts to limit the ion heating in a finite-sized turbulent region. The scattering increases the parallel velocities and lowers the average dwell time of an ion in the turbulent region. The nonthermal acceleration appears to be influenced by trapping, which randomly increases dwell time for some ions in the turbulent region. These conclusions must be verified by 3D simulations that include a background electric field and reversing magnetic fields.

### 5. Discussion

The measurements of  $E_{ac}$  in the turbulent region reveal a defined  $d_{corr}$ ,  $t_{corr}$ , and PDF for  $f > f_{ci}$ , which provides a representative reproduction of  $E_{ac}$  that has an excellent agreement with the measured PSD (the Appendix). This reproduction of  $E_{ac}$ , in turn, allows for a realistic test-particle simulation of electron energization. Electrons are magnetized in spite of the strong fluctuations in  $\mathbf{B}$  and, in the absence of a net  $\Phi_{||}$ , electron energization is dominated by  $E_{ac\perp}$ . The test-particle simulations are able to reproduce many of the observed features in the electron distributions. These simulations support the conclusion drawn from the  $\mathbf{J} \cdot \mathbf{E}$  measurements: perpendicular energization is dominant despite the fact that  $T_{e\parallel} > T_{e\perp}$  in the thermal core. The higher  $T_{e\parallel}$  is found to be from a “filtering” effect from random  $\Delta\Phi_{||}$  that preferentially excludes low- $W_{e\parallel}$  electrons from entering the turbulent region.

Nonthermal acceleration is promoted via disproportionately higher energization of higher-energy particles, which can be enabled by a variety of processes (Blandford & Eichler 1987). In the case of electrons, the highest  $v_{e\parallel}$  electrons can traverse  $d_{corr}$  in less time than the cyclotron period, so high  $v_{e\parallel}$  electrons receive higher perpendicular heating. However, we find that nonthermal acceleration of electrons is predominantly enabled by trapping in  $\mathbf{B}$  depletions. Electrons that experience perpendicular energization while passing through a  $\mathbf{B}$  depletion can be trapped. The trapped electrons accumulate and experience further perpendicular energization, which moves their pitch angles toward  $90^\circ$  and serves to strengthen their trapping. Thus, perpendicular heating and  $\mathbf{B}$  depletions conspire to effect a near runaway acceleration in test-particle simulations. The finite lifetime of  $\mathbf{B}$  depletions limits electron acceleration.

While electron energization is formidable, ions are the primary recipient of the net energy from  $\mathbf{J} \cdot \mathbf{E}$ . Analytic analysis and direct application of the measured  $\mathbf{E}$  and  $\mathbf{B}$  indicate the power in  $\mathbf{E}$  with  $f \leq f_{ci}$  or  $k\rho_i \sim 1$  dominates ion heating resulting in substantial  $\dot{W}_{i\perp}$  and weak  $\dot{W}_{i\parallel}$ . The inferred values of  $\dot{W}_{i\perp}$  from  $\mathbf{J} \cdot \mathbf{E}$ , large-scale modeling, and direct application of the measured  $\mathbf{E}$  and  $\mathbf{B}$  suggest heating rates of  $\sim 2 \text{ keV s}^{-1}$  to  $\sim 3 \text{ keV s}^{-1}$ , which would result in

$T_{i\perp} > 200 \text{ keV}$ , which is not seen in the measured ion distributions. We demonstrate that magnetic fluctuations ( $\delta\mathbf{B}$ ) can limit ion heating via pitch-angle diffusion that transfers  $W_{i\perp}$  to  $W_{i\parallel}$ , which, in turn, enables more rapid escape from the turbulent region.

The ion acceleration process is more difficult to model since  $\rho_i$  is larger than the correlation scales of  $\mathbf{E}$  and  $\mathbf{B}$ . Furthermore, ions may energize by drifting through reversing  $\mathbf{B}$ . A realistic simulation requires a reproduction of  $\mathbf{E}$  with power at DC to  $f \sim f_{ci}$  as well as  $\delta\mathbf{B}$ .  $\mathbf{E}(f < f_{ci})$  and  $\delta\mathbf{B}$  are not as well reproduced as in the case with  $E_{ac}$ . The rms power levels and the spectra are replicated, but intermittency (phase-coherent structure) is not reproduced. Nonetheless, the test-particle simulations suggest that trapping in a  $\mathbf{B}$  depletion promotes nonthermal acceleration.  $\delta\mathbf{B}$  has two opposing roles. On one hand,  $\delta\mathbf{B}$  promotes pitch-angle scattering that limits ion heating in a finite domain. On the other hand,  $\mathbf{B}$  depletions can trap ions and increase their dwell time in the turbulent region, which leads to nonthermal acceleration.

A primary question is how the observed acceleration processes scale with the size of the turbulent domain and the energies of the particles. While MMS observations are confined to a region ( $10^8 \text{ m}$ ) limited by the size of Earth’s magnetosphere, the powerful combination of trapping in magnetic depletions and perpendicular energization should scale to larger systems. The driving scale of turbulence is not naturally limited. Shocks in supernova remnants are known to be extensive ( $10^{16} \text{ m}$ ) as should be the turbulent regions nearby them.

This energization mechanism deserves further consideration for larger astrophysical systems. As emphasized earlier, the turbulent regions occupy far more volume than do shocks or magnetic reconnection diffusion regions. Regions of strong turbulence could be extensive or, as a minimum, many such regions could develop. Magnetic depletions appear to have a range of scale sizes, possibly up to the driving scale. It is possible then, that the limitations of energy gain due to the finite size as in the case of the Earth’s magnetosphere may not be as strongly realized.

The very nature of turbulence is to cascade energy from driving scales to dissipation scales, which, for most space and astrophysical environments, is at  $k\rho_i \approx 1$ ,  $kd_i \approx 1$ , and/or  $f \approx f_{ci}$ . For a high- $\gamma$  particles, the cyclotron heating rate (Equation (2)) can be estimated from Equation (7) by setting  $t_{corr} = 1/f_{ci}$  and realizing that only left-hand polarized ( $h_L$ ) power contributes:

$$\begin{aligned} \dot{W}_{i\perp} &\approx \eta_L \frac{e^2 t_c \langle |E_{ac}|^2 \rangle}{2W_{iR}/c^2} \approx \frac{e^2 \eta_L}{2W_{iR}/c^2} P_E(f_{ci}) \\ &= \frac{e^2 \eta_L}{2\gamma m_i} P_E(f_{ci}). \end{aligned} \quad (8)$$

As a reminder,  $P_E(f_{ci})$  is the PSD at  $f_{ci}$  and  $W_{iR} = \gamma m_i c^2$ . Equations (8) and (2) are identical in the classical limit. Since  $f_{ci} \propto \gamma^{-1}$  and  $P_E \propto f^{-1.25}$  in the inertial range (see Figure 2(d) of the companion paper),  $\dot{W}_{i\perp}$  increases mildly with increasing  $\gamma$  ( $\gamma^{0.25}$ ). As such, the primary acceleration process driven by turbulence (perpendicular heating combined with trapping in magnetic depletions of perpendicularly heated particles) may be active for high- $\gamma$  particles in large-scale systems. Further investigation is deserved.

## 6. Conclusions

The process of nonthermal acceleration has been of great interest ever since the discovery of cosmic rays and the acceleration of charge particles in a variety of space and astrophysical plasmas. The central conclusion of this investigation and that in the [companion paper](#) is that strong turbulence, that with magnetic depletions and large-amplitude electric fields, leads to the development of a nonthermal population of high-energy charged particles. Heating, of course, is expected from turbulence. In a turbulent environment, the driving energy, flow energy or magnetic field energy, cascades to larger wavenumber and/or higher frequencies until dissipation develops.

The energization processes of electrons and ions are distinct and quite complex, but they both indicate that perpendicular energization is dominant and that trapping in magnetic depletions enhances nonthermal acceleration. Cyclotron- and gyro-resonant energization appears to be a primary mechanism for ions and higher-frequency second order energization for electrons, but Fermi acceleration and betatron acceleration may be significant. Particle trapping in  $\mathbf{B}$  depletions appears to greatly enhance nonthermal acceleration. With perpendicular energization, a trapped particle continues to gain perpendicular energy, which leads to a lower probability of escape. The combination can result in a vigorous energization process (e.g., Figures 3(e) and 5(a)).

A finite lifetime of magnetic depletions, a diffusive-like process, or escape from the turbulent region limit the near runaway energization of charge particles trapped in a magnetic depletion. Interestingly, the development and collapses of magnetic depletions and magnetic holes (Goodrich et al. 2016a, 2016b) lead to the Fermi-like and betatron acceleration. Magnetic depletions undoubtedly must be considered in heating processes.

While the energies in the observed turbulent heating are relatively small ( $<1$  MeV) compared to the cosmic ray spectrum, the MMS observations provide good insight into the acceleration process. Heating from turbulence may be active in many astrophysical settings. Energetic particles emerge from the solar corona, which is known to be turbulent. Energetic particles are certainly expected in other turbulent stellar environments, in particular from M star and other active flare stars. Intriguingly, the environment of pulsar nebulae is very similar to that in the Earth's magnetotail;  $|\mathbf{B}|$  and  $n$  are roughly the same. Shocks and magnetic reconnection in the supernova shell may create similar or larger pockets of strong turbulence. Strong turbulence is also expected in shocked plasma jets.

The size of the region of strong turbulence as observed by MMS is limited to the size of Earth's magnetosphere. Turbulence, however, can develop on significantly larger scales; there is no natural limit. Alternatively, numerous regions of strong turbulence may be found in pockets surrounding magnetic reconnection sites and shocks. Turbulent domains, when active, are expected to have volumes many orders of magnitude larger than that occupied by the diffusion region of magnetic reconnection. The region of turbulence behind shock fronts also occupies significantly more volume than do the shock ramps. We point out that a mid-stage pulsar nebulae (several parsecs in size) has approximately  $10^{27}$  times the volume of Earth's magnetosphere. The dwell time of ions in a turbulent region could be increased by many orders of

magnitude, particularly under large-scale trapping. As such, particle acceleration within the turbulent regions could conceivably supply a significant population of energetic particles to, as a minimum, the low-energy part of the cosmic ray spectrum.

This work was funded by the NASA MMS project. The authors recognize the tremendous effort in developing and operating the MMS spacecraft and instruments and sincerely thank all involved. All of the data used in this article are publically available from the MMS Science Data Center.

## Appendix

### Details of Test-particle Simulations

The 1D/3D simulation domain extends from approximately  $-10 R_E$  to  $10 R_E$  with open boundaries (Figure 2(a)). At the boundaries, Maxwellian electron or ion distributions are set to the ambient temperature and a normalized density of unity. The simulation domains are initiated with the ambient distribution throughout ( $\sim 275,000$  particles). With open boundaries, particles enter and exit the simulation domain from (to) the ambient distributions at the boundaries. Particles that exit the simulation domain are removed. The time steps ( $\Delta t = 10^{-4}$  s for electrons and  $\Delta t = 10^{-2}$  s for ions) are set so that the fastest particles take several steps to traverse  $d_{\text{corr}}$ . The time step is empirically validated by reducing  $\Delta t$  to 1/2 of its nominal value, re-executing a simulation, then verifying that the results do not meaningfully change.

For each time step, particles are advanced in position and momentum using a Boris-like algorithm, which conserves energy of gyrating particles. The time steps are more than adequate with  $1/f_{ce} \sim 20 \Delta t$  and  $1/f_{ci} \sim 800 \Delta t$ . Execution of the code with  $\mathbf{B} = 20$  nT and  $\mathbf{E} = 0$  verifies less than 1% change in the domain-averaged temperature and density over long periods (60 s for electrons, 500 s for ions). Inside of the simulation domain, the particle distributions remain, within statistical deviations, identical to those imposed at the boundaries, which also verifies the boundaries are treated properly.

Particle motion in 3D in a 1D physical domain with changing  $\mathbf{B}(x)$ ; ( $x$  is distance) requires application of the magnetic mirror force,  $\mu \nabla_{\parallel} B_{\parallel}$ , for parallel motion combined with  $\mu$  conservation in the perpendicular motion. For each time step, the particle advancement has two parts. The first part evolves momentum using  $\mathbf{B}(x)$ . The mirror force is applied to the parallel motion and the perpendicular motion is adjusted conserving  $\mu$ . The second part advances momentum using  $\mathbf{E}$ , which can change  $\mu$  and/or energy. This approach is similar to that used in relativistic particle tracing in the Earth's radiation belts (e.g., Northrop 1963; Elkington et al. 2002, 2004). Energy conservation is tested via long-duration runs with a magnetic depletion (see Figure 3) with  $\mathbf{E} = 0$ . In these tests, trapped particles remain trapped and free particles pass the magnetic depletion. The energy change over long periods is less than 1%.

The development of the imposed  $\mathbf{E}$  is a key aspect of the simulation. For the electron simulations, the reproduction of  $\mathbf{E}$  is based on the statistical analysis of the observed  $\mathbf{E}_{ac}$  using the  $d_{\text{corr}}$ ,  $t_{\text{corr}}$ , and the measured PDF of  $E_{ac\parallel}$  and  $E_{ac\perp}$  (the [companion paper](#)). The turbulent region is divided into a series of  $\sim 3000$  contiguous segments, each with a physical length of  $d_{\text{corr}}$  plus/minus a random  $1\sigma$  variation of  $1/4 d_{\text{corr}}$ . Each of the segments is assigned a pseudo-random value of

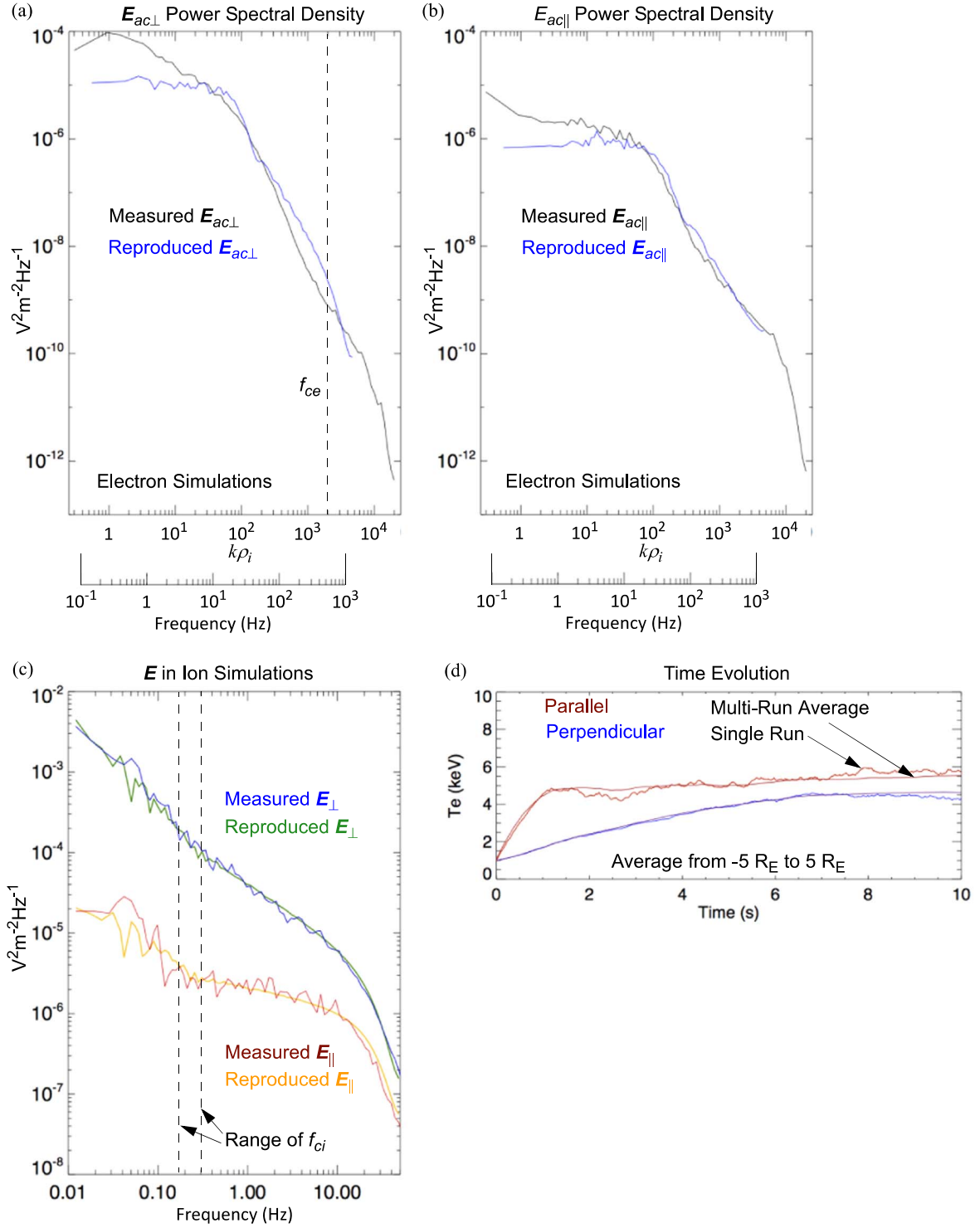


**Figure A1.** (a) A comparison of the PSD of the measured  $E_{ac\perp}$  to that of the reproduced  $E_{ac\perp}$ . (b) A comparison of the PSD of the measured  $E_{ac\parallel}$  to that of the reproduced  $E_{ac\parallel}$ . (c) PSDs of the measured  $E$  and the reproduced  $E$  used in the ion simulations. (d)  $T_{e\parallel}$  and  $T_{e\perp}$  as a function of time from a single run (noisy trace) and averaged over 25 runs (smooth trace).

$E_{\parallel}$  and  $E_{\perp}$  that statistically reproduce the shape of the measured PDFs of  $E_{\parallel}$  and  $E_{\perp}$ . In Figures 1(l) and (m), the black trace is the measured PDF and the gold trace is the reproduced PDF.  $E_{\perp}$  is assigned a random direction in each segment. Each component of  $E(x)$  is smoothed over  $\sim 3$  km to remove sharp edges. The turbulent region extends from  $-8 R_E$  to  $8 R_E$  with smooth edges with a thickness of  $1/2 R_E$  so  $E = 0$  if within  $1.75 R_E$  of the boundaries of the simulation.

As the simulation progresses,  $E(x)$  remains constant in time for a period of  $t_{corr}$  plus a random  $1\sigma$  variation of  $1/4 t_{corr}$ . Once the time period ( $240 \pm 60 \Delta t$ ) is nearly expired,  $E_{\parallel}$  and  $E_{\perp}$  are regenerated (segment lengths are also updated).  $E(x)$  evolves from the previous array to the regenerated array over 0.5 ms to avoid abrupt time changes.


Figures A1(a) and (b) show the measured and reproduced  $E_{ac}$  spectra. The black traces are the measured  $E_{ac\perp}$  spectra (the

native spectra are time-domain). The dashed blue lines are the spectra of the raw reproduced  $E_{\parallel}$  and  $E_{\perp}$  (the native spectra are spatial domain). The reproduced spectra reasonably match the measured spectra (Figures A1(a) and (b)), which adds support to the assumption that the measured  $E_{ac}$  is from random fluctuations. The reproduced  $E_{ac}$  has the same  $d_{corr}$ ,  $t_{corr}$ , PDF, rms power, and spectral shape of the measured  $E_{ac}$ .

For the ion test-particle simulations,  $E$  is reproduced as a time series by reproducing the observed spectra (Figure A1(c)). A set of 10,000 waves with random frequencies from 0.01 to 50 Hz are generated. The ion simulations have  $\Delta t = 10^{-2}$  s, so  $f$  cannot exceed 50 Hz. The amplitudes of the waves are pseudo-random to match the observed PSD.  $E_{\parallel}$  and the two components of  $E_{\perp}$  are generated separately and are assigned random phases at  $t = 0$ . A unique time series of  $E$  is developed for each ion.  $\delta B$  is developed in a similar fashion. However, all components of  $\delta B$  are generated to match the total spectra (Figure 3(d) of the companion paper).

As a final note, the plots of  $T_{e\parallel}$  and  $T_{e\perp}$  in Figures 2–4 are averaged over multiple runs. Minor variations in  $T_{e\parallel}$  and  $T_{e\perp}$  as a function of distance or time come from statistical noise due to the limited number of test particles. However, stronger variations in  $T_{e\parallel}$  (and to a lesser degree, in  $T_{e\perp}$  and  $n_e$ ) are from the intermittent development of large-amplitude  $E_{\parallel}$  signals. These variations are not statistical noise. Intermittent, large-amplitude  $E_{\parallel}$  events mimic actual observations and, in fact, are a characteristic of turbulence. Increasing the number of test particles does not remove such variations in  $T_{e\parallel}$  and  $T_{e\perp}$ . Averaging over many runs, however, does remove the variations since the intermittent development of large-amplitude  $E_{\parallel}$  signals does not occur at the same positions or same times in separate runs. Multi-run averaging better isolates a characteristic  $T_{e\parallel}$  and  $T_{e\perp}$  response. Figure A1(d) shows an example of a single run (noisy trace) versus a 25-run average (see Figure 2(e)). In particular, the consequence of Fermi and betatron acceleration (Figures 4(b) and (f)) is much more easily discerned via a multi-run average.

### ORCID iDs

R. E. Ergun  <https://orcid.org/0000-0002-3096-8579>  
 P. A. Cassak  <https://orcid.org/0000-0002-5938-1050>  
 J. E. Stawarz  <https://orcid.org/0000-0002-5702-5802>  
 W. H. Matthaeus  <https://orcid.org/0000-0001-7224-6024>  
 J. F. Drake  <https://orcid.org/0000-0002-9150-1841>  
 M. A. Shay  <https://orcid.org/0000-0003-1861-4767>  
 J. L. Burch  <https://orcid.org/0000-0003-0452-8403>

### References

Alexandrova, O., Lacombe, C., Mangeney, A., Grappin, R., & Maksimovic, M. 2012, *ApJ*, **760**, 121  
 Andersson, L., Ergun, R. E., Newman, D. L., et al. 2002, *PhPI*, **9**, 3600  
 Arons, J. 2012, *SSRv*, **173**, 341

Blandford, R., & Eichler, D. 1987, *PhR*, **154**, 1  
 Boris, J. P. 1970, in Proc. 4th Conf. Numerical Simulation of Plasmas, Relativistic Plasma Simulation-optimization of a Hybrid Code (Washington, DC: Naval Res. Lab.), 3  
 Borovsky, J. E., Elphic, R. C., Funsten, H. O., & Thomsen, M. F. 1997, *JPLPh*, **57**, 1  
 Breuillard, H., Matteini, L., Argall, M. R., et al. 2018, *ApJ*, **859**, 127  
 Burch, J. L., Moore, T. E., Torbert, R. B., & Giles, B. L. 2016, *SSRv*, **199**, 5  
 Chang, T., Crew, G. B., Hershkowitz, N., et al. 1986, *GeoRL*, **13**, 636  
 Chasapis, A., Retino, A., Sahraoui, F., et al. 2015, *ApJL*, **804**, L1  
 Chevalier, R. A. 1977, *ARA&A*, **15**, 175  
 Cranmer, S. R., Asgari-Targhi, M., Miralles, M. P., et al. 2015, *RSPTA*, **373**, 20140148  
 Drake, J. F., Swisdak, M., Che, H., & Shay, M. A. 2006, *Natur*, **443**, 553  
 Eastwood, J. P., Phan, T. D., Bale, S. D., & Tjulin, A. 2009, *PhRvL*, **102**, 035001  
 Egedal, J., Daughton, W., Le, A., & Borg, A. L. 2015, *PhPI*, **22**, 101208  
 Elkington, S., Hudson, M., Wiltberger, M., & Lyon, J. 2002, *JASTP*, **64**, 233  
 Elkington, S., Wiltberger, M., Chan, A., & Baker, D. 2004, *JASTP*, **66**, 1371  
 Ergun, R. E., Ahmadi, N., Kromyda, L., et al. 2020, *ApJ*, **898**, 154  
 Ergun, R. E., Andersson, L., Tao, J., et al. 2009, *PhRvL*, **102**, 155002  
 Ergun, R. E., Goodrich, K. A., Stawarz, J. E., Andersson, L., & Angelopoulos, V. 2015, *JGR*, **120**, 1832  
 Ergun, R. E., Goodrich, K. A., Wilder, F. D., et al. 2018, *GeoRL*, **45**, 3338  
 Ergun, R. E., Malaspina, D. M., Bale, S. D., et al. 2010, *PhPI*, **17**, 072903  
 Ergun, R. E., Tucker, S., Westfall, J., et al. 2016, *SSRv*, **199**, 167  
 Goldreich, P., & Sridhar, S. 1995, *ApJ*, **438**, 763  
 Goldstein, M. L., Roberts, D. A., & Fitch, C. A. 1994, *JGR*, **99**, 11519  
 Goodrich, K. A., Ergun, R. E., & Stawarz, J. E. 2016a, *GeoRL*, **43**, 6044  
 Goodrich, K. A., Ergun, R. E., Wilder, F. D., et al. 2016b, *GeoRL*, **43**, 5953  
 Gosling, J. T., Asbridge, J. R., Bame, S. J., Paschmann, G., & Scokopke, N. 1978, *GeoRL*, **5**, 957  
 Gosling, J. T., Thomsen, M. F., Bame, S. J., & Russell, C. T. 1989, *JGR*, **94**, 10027  
 Huang, S. Y., Sahraoui, F., Yuan, Z. G., et al. 2017, *ApJL*, **836**, L27  
 Jaynes, A. N., Turner, D. L., Wilder, F. D., et al. 2016, *GeoRL*, **43**, 7356  
 Le Contel, O., Leroy, P., Roux, A., et al. 2016, *SSRv*, **199**, 257  
 Lindqvist, P.-A., Olsson, G., Torbert, R. B., et al. 2016, *SSRv*, **199**, 137  
 Marchand, R., Miyake, Y., Usui, H., et al. 2014, *PhPI*, **21**, 62901  
 Matthaeus, W. H., Ambrosiano, J. J., & Goldstein, M. L. 1984, *PhRvL*, **53**, 1449  
 Mauk, B. H., Blake, J. B., Baker, D. N., et al. 2016, *SSRv*, **199**, 471  
 Nagai, T., Fujimoto, M., Saito, Y., et al. 1998, *JGR*, **103**, 4419  
 Newman, D. L., Goldman, M. V., Ergun, R. E., & Mangeney, A. 2001, *PhRvL*, **87**, 255001  
 Northrop, T. G. 1963, *RvGSP*, **1**, 283  
 Øieroset, M., Lin, R. P., Phan, T. D., Larson, D. E., & Bale, S. D. 2002, *PhRvL*, **89**, 19195001  
 Øieroset, M., Phan, T. D., Fujimoto, M., Lin, R. P., & Lepping, R. P. 2001, *Natur*, **412**, 414  
 Oka, M., Birn, J., Battaglia, M., et al. 2018, *SSRv*, **214**, 82  
 Pollock, C., Moore, T., Jacques, A., et al. 2016, *SSRv*, **199**, 331  
 Price, L., Swisdak, M., Drake, J., et al. 2016, *GeoRL*, **43**, 6020  
 Price, L., Swisdak, M., Drake, J., et al. 2017, *JGR*, **122**, 11086  
 Quataert, E., & Gruzinov, A. 1999, *ApJ*, **520**, 248  
 Russell, C. T., Anderson, B. J., Baumjohann, W., et al. 2016, *SSRv*, **199**, 189  
 Schwartz, S. J., & Burgess, D. 1991, *GeoRL*, **18**, 373  
 Speiser, T. W. 1965, *JGR*, **70**, 4219  
 Stawarz, J. E., Eriksson, S., Wilder, F. D., et al. 2016, *JGRA*, **121**, 11021  
 Torbert, R. B., Burch, J. L., Phan, T. D., et al. 2018, *Sci*, **362**, 1391  
 Torbert, R. B., Russell, C. T., Magnes, W., et al. 2016, *SSRv*, **199**, 105  
 Turner, D. L., Wilson, L. B., Liu, T. Z., et al. 2018, *Natur*, **561**, 206  
 Weygand, J. M., Kivelson, M. G., Khurana, K. K., et al. 2005, *JGR*, **110**, A01205